

## X-ray Diffraction of Bent Crystals in Bragg Geometry. II. Non-ideally Imperfect Crystals, Modelling and Results

BY C. T. CHANTLER\*

*Clarendon Laboratory, University of Oxford, Parks Road, Oxford OX1 3PU, England*

(Received 23 April 1991; accepted 5 May 1992)

### Abstract

An earlier model for finite curved perfect crystals is extended to the non-ideally imperfect regime, allowing for mosaic structure from dislocations, vacancies or phase boundaries. Effects of Johann crystal mounting and depth penetration in the Bragg geometry are included. The model estimates diffraction shifts for mosaic crystals with regular local structure. Integrated reflectivities, diffraction widths, shifts and profiles against several parameters demonstrate agreement with the earlier model as an extreme and hence agreement with the literature. The theory is applied to first- and fourth-order spectra in differential quantum electrodynamic (QED) measurements and to pentaerythritol 002 crystals. A study of widths, reflectivities and shifts shows that comparison of profiles from wavelengths differing by large factors can yield the mean mosaic block thickness, angular misorientation half-width, incident polarization and beam divergence and can provide sensitive experimental tests of theory and modelling. Results for ammonium dihydrogen phosphate 101 and silicon 111 crystals agree with experiment for parameters investigated. Qualitative contributions to shifts and other parameters are identified. Results for precision QED measurements of iron and germanium Lyman  $\alpha$  and Balmer  $\beta$  radiation are presented. Uncertainties in shifts due to input parameters are provided for each crystal. Crystal thickness can be a major variable in the determination of diffraction shifts, and differences between perfect and mosaic crystals are reduced for curved crystals.

### 1. Mosaic effects

Many crystals demonstrate behaviour at variance with perfect-crystal diffraction, with integrated reflectivities and diffraction half-widths exceeding theoretical values by an order of magnitude and variations

of this order of magnitude between crystals of the same species prepared under different conditions (Zachariasen, 1945).

These effects are due to lattice imperfections, interstitials, substitutions, vacancies and polymorphism. Models do not treat all crystal imperfections, but relate to assumed dominant imperfections in most real crystals. This is understood as mosaic stacking of crystallites within each crystal. Substitutional and interstitial defects are neglected in such treatments as they represent a crystal with different atomic form factors.

Copper, silicon and germanium rocking curves show deviation from perfect-crystal theory for dislocation densities at  $10^4 \text{ cm}^{-2}$  while integrated reflectivities are unaltered until values of  $2 \times 10^5 \text{ cm}^{-2}$  are exceeded, reaching the mosaic limit at densities of the order of  $10^7 \text{ cm}^{-2}$  (Bachman, Baldwin & Young, 1970; Patel, Wagner & Moss, 1962; Batterman, 1959). This suggests that mosaic behaviour is dominant for block dimensions of less than  $3 \mu\text{m}$ . This relates to unstressed flat crystals and Cu  $K\alpha$  radiation (8 keV), varying by an order of magnitude for crystals prepared under other conditions or illuminated with Mo  $K\alpha$  X-rays (17.5 keV). Mosaic behaviour may only dominate for LiF 200 crystals and 6 keV X-rays for dislocation densities of  $5 \times 10^{10} \text{ cm}^{-2}$  or block dimensions less than  $0.05 \mu\text{m}$  (Brown, Fatemi & Birks, 1974).

### 2. Semi-empirical relations

Crystallites are assumed equivalent to thin perfect (and flat) parallelepiped units of thickness  $t_0$  in a plane-parallel crystal of thickness  $T$  with the normal of the diffracting planes forming a statistical distribution about some mean value. A Gaussian distribution of these angles is given by

$$W(\Delta) = [(\ln 2)^{1/2}/(\eta\pi^{1/2})] \exp [-(\ln 2)\Delta^2/\eta^2], \quad (1)$$

where  $W$  is the probability of deviation from the mean value,  $\Delta$  is the angular misorientation and  $\eta$  is the distribution half-width. Ideal mosaic or ideally imperfect crystals have negligible primary and

\* Present address: Quantum Metrology Division, National Institute of Standards and Technology, Gaithersburg, MD 20899, USA.

secondary extinction, so (i) attenuation of incident beams through a single crystallite by diffraction is negligible compared with absorption and (ii) diffracted (reflected) waves from one crystallite are unaffected by diffraction from other crystallites (owing to large angular deviations between crystallites and the dominance of absorption). Standard treatments assume that the diffraction profile is dominated by the mosaic angular distribution, or by the perfect-crystal (mosaic-block-size) extreme. On this basis, the integrated reflectivity of flat crystals for a given incident polarization is (Burek, Barrus & Blake, 1974; Caciuffo, Melone, Rustichelli & Boeuf, 1987)

$$\begin{aligned} R_H^{\theta, \text{mosaic}} &= (e^2/m^2c^4)/[N^2\lambda^3/(2\mu \sin 2\theta)]|CF_H|^2 \\ &= [|C\psi_H|/(\sin 2\theta_B)]R_H^y, \\ R_H^{y, \text{mosaic}} &= \pi/(4|g|) = \pi|C\psi_H|/(4|\psi_0''|). \end{aligned} \quad (2)$$

The symbols have the same meaning as in paper I (Chantler, 1992). Semiempirical extension of formulae for integrated reflectivities in ideal mosaic crystals to cases of intermediate perfection raises problems from kinematic limitations of mosaic approximations and from others inherent in the mosaic model (Becker & Coppens, 1974; Brown & Fatemi, 1974). The latter authors suggested a flat-crystal symmetric Bragg reflection form. The value of  $g$  therein may be generalized here to asymmetric Bragg diffraction using

$$\begin{aligned} R_H^{\theta} &= R_H^{\theta, \text{mosaic}}(-g)/\{\exp[g - \ln(32/3\pi)] - g\}, \quad (3) \\ g &= [(1-b)/(2|b|^{1/2})]/\{8\mu R_H^{\theta, \text{mosaic}}[\alpha\bar{t} + \alpha'(\bar{T}-\bar{t})]\}^{1/2}. \end{aligned} \quad (4)$$

The  $\alpha$  and  $\alpha'$  contributions relate to primary and secondary extinction, respectively, and the mean path length through a mosaic block (in Bragg reflection, neglecting diffraction/extinction) is given by the normalized values

$$\begin{aligned} \bar{t} &= \left[ \int_0^a \exp(-\mu x) x dx \right] / \left[ \int_0^a \exp(-\mu x) dx \right] \\ &= 1/\mu - a \exp(-a\mu)/[1 - \exp(-a\mu)], \\ a &= t_0/(\sin \theta_{\text{inc}}) + t_0/(\sin \theta_{\text{out}}), \quad (5) \\ \alpha' &= \alpha/(1 + \{[4\pi^{1/2}/(3\eta)]\alpha\}^2)^{1/2}, \quad \alpha = \bar{t}(\sin 2\theta)/\lambda. \end{aligned} \quad (6)$$

This approaches values quoted by Brown & Fatemi (1974) for large absorption or block sizes ( $\bar{t} = \mu^{-1}$ ) or for small mosaic units and symmetric reflection [ $\bar{t} = t_0/(\sin \theta)$ ].  $\bar{T}$  is defined similarly, with  $t_0$  replaced by  $T$  in the above equation, and  $\alpha'$  includes a measure of block misalignment. The non-centrosymmetric perfect thick crystal solution (Cole & Stemple, 1962) with  $s$ ,  $p$  and  $\kappa$  as defined therein may be extended

similarly, using  $g$  as above,

$$\begin{aligned} R_H^y &\simeq (\pi/4)(1 + \kappa^2 + 2s)/(|g| + \exp\{-[(1 - \kappa^2)^2 \\ &\quad + 4p^2][|g| + \ln(32/3\pi)]\}). \end{aligned} \quad (7)$$

This yields Darwin behaviour for perfect non-absorbing crystals and mosaic behaviour for perfect crystals with large values of absorption and  $|g|$  for crystals with small block sizes (or large angular distributions) and for thin crystals. This reflects the increasing importance of absorption *versus* extinction (diffraction) processes. The result is limited to flat crystals, with *ad hoc* assumptions regarding extension to intermediate regimes.

Kato (1980a) has initiated an alternative description of mosaicity. This statistical dynamical theory treats defects and thermal oscillations as a distribution from which expectation values for interval wave fields may be derived. Two order parameters are involved: an intrinsic correlation length corresponding to the mean mosaic-block thickness and a Debye-Waller parameter relating to long-range perfection (or mean random deviation). This treats coherent and incoherent diffracted intensities in a coupled way, avoiding use of regular physical mosaic blocks. Secondary parameters are the distribution function and a correlation length of the incoherent intensity.

Application to flat-crystal Laue diffraction (Kato, 1980b) is difficult with undetermined parameters (Al Haddad & Becker, 1988; Guigay, 1989) and is designed for spherical incident waves and integrated reflectivities rather than profiles (Bushuev, 1989) and allows only continuous displacement fields as opposed to mosaic blocks (Punegov, 1990). The secondary correlation length is of the same order as the first, as opposed to earlier versions of the theory (hence corresponding to the same mosaic block size) (Becker & Al Haddad, 1990). While considerable progress is being made, the physical assumptions are questionable and do not apply to curved crystals.

Curvature reduces extinction and peak reflectivity while extending angular ranges over which diffraction can occur (in appropriate geometries), with a maximum lamellar thickness limiting coherence as discussed in paper I. Neglect of absorption gives the mean penetration depth  $T'_0 = 4|g|T$  (Hirsch & Ramachandran, 1950) and the approximate results for thick flat crystals (without or with extinction) of

$$T_0 = \mu^{-1}(1/\sin \theta_{\text{inc}} + 1/\sin \theta_{\text{out}})^{-1}, \quad (8)$$

$$T'_0 = T_0/[1 + 1/(4|g|)]. \quad (9)$$

For curved crystals, the extinction component due may drop by an order of magnitude (by the lamellar thickness and the change of diffracting angle with depth) and may increase the mean depth accordingly. This effect must be estimated precisely. Brown & Fatemi (1974) estimate part of this effect. Reflectivities

could be understood in terms of block sizes and width parameters that could not easily be measured, related to real crystals or directly tested. The present article is concerned with profiles and refractive-index shifts in curved crystals, not addressed by the above authors, in addition to integrated reflectivities.

### 3. Extension of finite curved perfect crystal model to include mosaic character

Mosaic models assume that crystallites are sufficiently small and evenly distributed that profiles are given by the mean of a statistical ensemble of crystallites at varying angles and widths. Angular distribution widths are assumed larger than rocking-curve widths, so individual blocks diffract independently. If crystallites have displacement disorders of arbitrary size but large compared with X-ray wavelengths, the phase relationship between the scattering of adjacent blocks will be random, so blocks will appear to diffract independently.

The mean Bragg plane is defined by  $\alpha_{\text{plane}}$  and the curvature of the crystal, so the primary effect on profiles is to convolve them with the mosaic distribution function. It is symmetric since stresses of curvature (inducing mosaicity) are symmetric and in our case  $\alpha_{\text{plane}} \approx 0$  so growth-induced mosaicity should also be symmetric. A Gaussian mosaic angular distribution is used in the current implementation. Lorentzian functions may be more appropriate, but the form contributes no shift. The mosaic angular half-width  $\eta$  affects shifts by increasing layers and crystal regions contributing to the final profile; this is a small shift, insensitive to small changes in  $\eta$ .

The major effect on profiles is due to the size (thickness) of the mosaic unit. Mosaicity has been neglected in earlier Lyman  $\alpha$  measurements (see, for example, Laming *et al.*, 1988) but is necessary to understand experimental results for these crystals. Mosaic blocks have a distribution of thicknesses, characterized by a single mean value. The block limits the coherence and interference depth in the crystal. Any perfect-crystal lamellae with thicknesses greater than the mosaic value will be subdivided. If the perfect-crystallite depth is less than the mosaic unit, radiation will diffract as if the crystal were perfect with a convolution for the angular distribution.

Mosaic structure is implemented by computing the perfect finite flat crystal thickness and profile for the given curvature and radiation, as described in paper I. This thickness is reduced to that of the mosaic block (recalculating the profile) as necessary. This perfect-but thin-crystal profile is convolved with the angular misorientation distribution to give the diffraction profile for a mean layer. Ray tracing using this mean profile over source, angle, layers and regions yields the final results (Fig. 1; *cf.* Fig. 8 in paper I). Care

must be taken in convolving very broad or narrow profiles with the mosaic angular distribution to adequate precision and continuity.

This method assumes that mosaic units are deformed cylindrically by the stress to the given curvature. Reduction in stress occurs by plastic deformation of the crystallite interface but the curvature should have the correct mean orientation. Glide-plane displacements may reduce local curvature, but asymmetric distortion from this source is assumed negligible. Anisotropic materials suffer additional curvature for planes not normal to the surface, but the present (symmetric) Bragg diffraction geometry minimizes or eliminates this effect (Kalman & Weissman, 1983).

Flat-crystalline diffracting units used should be curved for perfect curved crystals if the stress acts uniformly. Lattice positions may be deformed from unstressed values and form factors may be restricted and directed by this curvature. For crystallite thicknesses below  $5 \mu\text{m}$ , the phase difference of internal waves from curvature across the unit is less than  $\pi/4$ , so has little effect on diffraction. This scales by the square of the thickness, so periodic regions of large (0.1 mm) crystallites are out of phase compared with the flat-crystallite model. Diffraction in this (first-order) case is dominated by the first few lattice sites, minimizing effects. Locations of *Pendellösung* oscillations may be altered for near-perfect crystals. The  $2d$  spacing for a perfect crystal changes but, for  $2d = 8.7358 \text{ \AA}$  and  $2Rz = 300 \text{ mm}$ , the fractional change is below 0.04 in  $10^6$  and results are unaffected. Mosaic crystals have smaller shifts, with more rectangular crystallites.

Convolution with the angular distribution involves a second assumption, that any local region of a layer will have a range of orientations of crystallites, so the

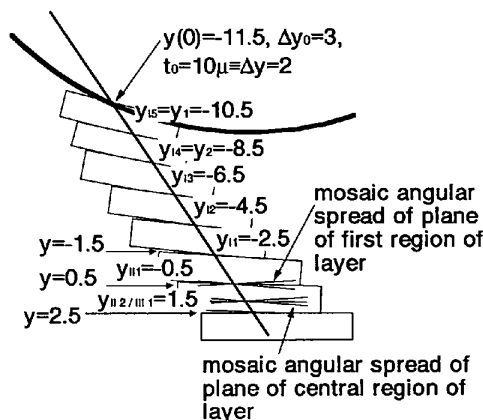


Fig. 1. Inclusion of mosaic imperfection, showing limitation of curved-lamellae thicknesses  $\Delta y_0$  by the mean mosaic unit thickness  $t_0$  and the convolution of the finite flat crystal profile with the angular distribution (*cf.* paper I, Fig. 8).

front area of each crystallite should be small. If crystallites are each of large area, this method will still give the correct 'average' profile but there may be significant local deviations and crystallite-induced asymmetry in final profiles.

Primary extinction is accounted for here, as opposed to earlier mosaic extensions and formulae. Secondary extinction is dealt with for the incident ray through the crystal. Following paper I, it is neglected for the ray diffracted from each crystallite. Lamellae adjacent to the peak diffracting unit contribute negligibly since this (and not  $\Delta y_0 = 2$ ) is the defining condition of perfect-crystallite thicknesses. Profile tails are affected by this but dominant contributions to the peak and 10th- to 90th-percentile regions are given to high accuracy. Where the bending radius is large (e.g.  $2Rz > 3$  m), the perfect-crystal model used larger lamellar thicknesses to allow for coherence lengths. If a mosaic thickness is much smaller than this thickness, the effect is large only over the diffraction peak (broadened by the angular convolution). The loss of intensity of the diffracted beam may be approximated by the symmetric case where  $P_n/R_n = T_{n-1}/P_0$ , by comparison with Fig. 1 of paper I. This neglects further multiple diffraction, which is small and incoherent with the primary beam. Mosaic phase shifts from dislocations or other disorder also eliminate coherence between crystallites.

The main divergence from an implementation of the 'statistical dynamical theory' may result from the neglect of coupling between wavefields or, equivalently, the assumption that the two coherence lengths are equal and coincide with the mean mosaic-block thickness. Inclusion of local angular distributions of crystallites may have an effect. The use of regular physical blocks is not a limitation because the depth and orientation of each block is random and statistically distributed. The angular width and mosaic thickness are generally unknown, especially for a random crystal. However, they may be estimated from flat-crystal diffraction profiles and integrated reflectivities, if available, or from typical values and dimensions.

#### 4. Computation of finite curved imperfect crystal model

Mosaic calculations are precision limited by a CPU time constraint; accordingly, the number of regions depends on the block size, order of diffraction and polarization. Typically, one region per block or layer yields adequate precision for thicknesses less than 1  $\mu\text{m}$ , requiring between 2 and 20 regions for larger blocks. High orders penetrate the crystal and more layers are involved in the calculations. Fourth-order radiation penetrates the full PET 002 crystal depth so is angle-dependent. The number of significant layers

increases with the path length through the crystal

$$\begin{aligned} \Delta y_{\max} &\approx [|b|^{1/2} (\sin 2\theta_B)/(C|\psi'_H|)]\Delta\theta \\ &\approx [|b|^{1/2} 2(\cos^2 \theta_B)/(C|\psi'_H|)]T/(2Rz). \end{aligned}$$

Steps used over estimated ranges of  $\theta_s$  and  $x$  (the source distribution) are therefore reduced from paper I for mosaic calculations. Fourth-order  $\sigma$ -polarization calculations are expensive in time (CPU) near  $45^\circ$  where the damping term  $\cos 2\theta \rightarrow 0$ , approximately as  $(\cos 2\theta)^{-3/4}$ .

Tests discussed in paper I show convergence of final profiles and reflectivities. Thin flat and finite curved imperfect crystal profiles for pentaerythritol (PET) 002 diffraction are plotted against angle and film location in Figs. 2 and 3 for mean mosaic-block thicknesses from 0.7 to 0.5  $\mu\text{m}$ . *Pendellösung* oscillations are much larger than those in Figs. 12 and 13 of paper I, arising from the narrow block width, especially for first-order diffraction. Flat-crystal angular widths have increased by factors of five, peak reflectivities have dropped and effects of precision on convolutions and ray tracing are noticeable for particular orders and polarizations.

Effects of changes of the input precision on profiles may indicate convergence and uncertainty. Tails and regions far from the peak are affected; but ranges are symmetric, covering reflectivities two orders of magnitude lower than peak values and peak heights and profiles are unaltered. Integrated reflectivities may be reduced by 1% but shifts and central profiles have converged. The main effect of decreasing the block thickness from 0.7 to 0.5  $\mu\text{m}$  is the uniform broadening of first-order radiation, coupled at the

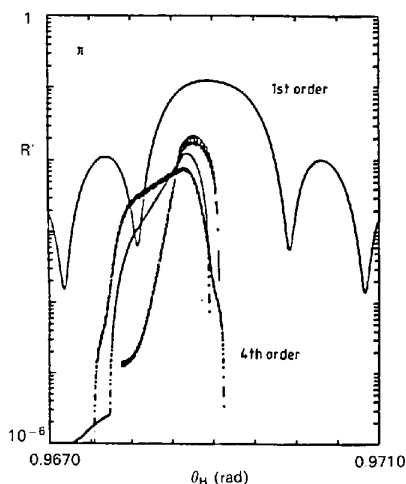


Fig. 2. Finite curved imperfect crystal profiles for PET 00(2n), 7.2  $\text{\AA}/n$ ,  $n = 1-4$ ,  $2Rz = 300$  mm,  $t_0 = 0.7$   $\mu\text{m}$ ,  $T = 0.4$  mm, angular half-width  $\eta = 5 \times 10^{-5}$  rad, plotted against grazing-emission angle  $\theta_2$  (non-normalized);  $\pi$  polarization, illustrating *Pendellösung* oscillation, depth penetration and calculation imprecision in profile tails.

lower limit with a broadening of fourth-order  $\sigma$ -polarized radiation. Other angles and orders show similar behaviour.

### 5. Spectrometer, beam and diffraction contributions to widths

Effects of finite crystallite widths, depth penetration, emulsion penetration and finite source size on angular and detector (photographic) widths, shifts and integrated reflectivities are illustrated in Table 1 for the case of  $2Rz = 300$  mm,  $T = 0.4$  mm,  $\lambda = 7.2 \text{ \AA}/n$ ,  $n = 1$  to 4,  $\theta_B = 0.969$  rad and diffraction from PET 00( $2n$ ) crystals in the geometry of paper I. Different orders are sensitive to different effects. Table 1 indicates effects of varying block thickness and angular distribution on these parameters. Shifts vary little over the wide range of block thicknesses, but widths and reflectivities vary greatly.

Each group of rows corresponds to a separate set of mosaic parameters, while each row gives results of a particular test as discussed in paper I, corresponding to the control parameter given in column '\*'. Thus, (–1) gives values for the finite flat perfect crystal case, (0) gives the finite flat crystal case where the thickness

is determined by the perfect-crystal curvature or [as in (6)] limited by the mosaic-block thickness and convolved with the angular distribution, (1) gives the curved-crystal result in the Rowland-circle geometry if a point source and surface diffraction are assumed, (2) and (3) include, respectively, the effect of a thicker crystal and that of a finite source, (4) indicates detector (emulsion) penetration and (5) includes all these effects (in this case, for a curved perfect crystal).

Table 1(a) compares angular widths from flat-crystal diffraction in a non-Rowland-circle geometry with the current set-up. First-order  $\pi$  radiation is much broader than  $\sigma$  radiation and (ideal) Rowland-circle geometry, defocusing, depth penetration and finite source in the curved perfect crystal case have minor effects. Fourth-order radiation is broadened ten times by finite crystallite thickness from the curvature and another twenty times by depth penetration. The latter is negligible for first-order radiation but dominates for fourth-order radiation until the mosaic-block thickness is reduced to  $0.70 \mu\text{m}$  or the angular width reaches  $10^{-4}$  rad.

Block widths greater than curved perfect crystallite values  $t_0$  given in Table 1(b) have no effect, so the range of mosaic thicknesses varies from this down to the minimum ordering of  $0.001 \mu\text{m}$  of two adjacent unit cells. Only mosaic-block thicknesses much smaller than perfect-crystallite values show significant deviation from perfect-crystal behaviour. Research concluding that crystals are 'perfect' from width measurements may neglect mosaic character revealed with a different curvature or wavelength. Here,  $t_0 = 50 \mu\text{m}$  is equivalent to a perfect curved crystal. First- and second-order radiation show broadening for  $t_0 = 5 \mu\text{m}$ , owing to flat-crystal profiles. The near-perfect regime  $t_0 > 5 \mu\text{m}$  cedes to an intermediate regime down to  $t_0 \approx 0.4 \mu\text{m}$  where first- (but not fourth-) order radiation is broadened by an order of magnitude. Below this, both orders broaden rapidly towards ideally imperfect limits.

Angular widths may be given in  $\mu\text{m}$  on the detector ( $Y_{iz}$ ) scale, confirming that  $10^{-5}$  rad broadening is negligible for PET 002, but that angular widths twenty times greater than this dominate diffraction profiles except for block thicknesses of less than  $1 \mu\text{m}$ . Lamellar thicknesses for perfect crystals decrease with increasing order and are larger for  $\pi$ -polarized radiation. This trend is also observed in widths at the detector for a point source and a single-lamella crystal. Widths are broadened uniformly by the finite source and the trend is reversed by depth penetration. The mosaic angular distribution broadens all orders uniformly (within the current model) while the mean block thickness broadens lower orders more.

Finite precision in calculations can lead to large errors in widths without affecting shifts, noted with a '+' in Table 1. Precision is reduced as the

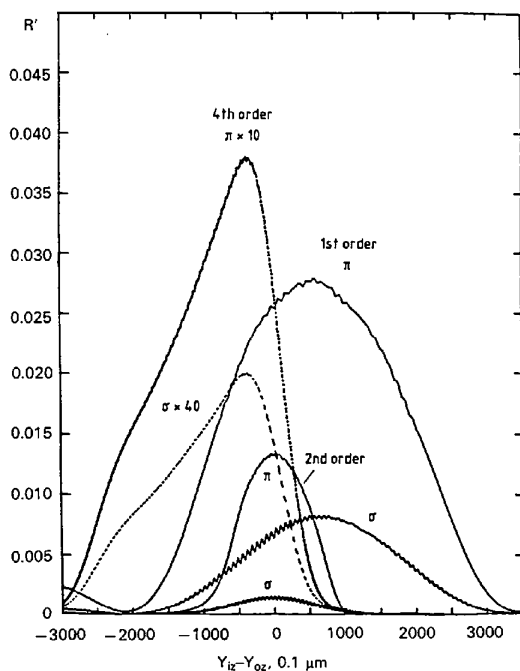


Fig. 3. Expected real profiles on the detector scale (relative to point-source surface Bragg diffraction location  $Y_{0z}$ ) for PET 00( $2n$ ) finite curved imperfect crystal diffraction at  $7.2 \text{ \AA}/n$ ,  $n = 1, 2, 4$ , scaling fourth-order diffraction by  $(10 \times, 40 \times)$  for  $(\pi, \sigma)$ . The crystal thickness is  $0.4$  mm. Mosaic-block width  $t_0 = 0.7 \mu\text{m}$  and angular half-width  $\eta = 5 \times 10^{-5}$  rad.

mosaic-block size is reduced. Mosaic-block thicknesses of  $t_0 = 0.75$  to  $0.70 \mu\text{m}$  give estimated width uncertainty on the detector  $Y_{iz}$  scale of  $\pm 1 \mu\text{m}$ , while  $t_0 = 0.65$  to  $0.50 \mu\text{m}$  leads to a FWHM of about  $\pm 3 \mu\text{m}$ . The effect of thickness on the broadening of different orders is seen by comparison of row (27) with (27b).

### 6. Contributions to centroid shifts and reflectivities, and mosaic limits

Refractive-index corrections dominate centroid shifts (on the detector scale) for first-order radiation, while fourth-order radiation is dominated by depth penetration and the crystal thickness. This is indicated in Table 1(c) by comparison of rows (27) and (27b). The finite source, Rowland-circle geometry, emulsion shifts and mosaic-block thickness play minor roles but are most significant for second-order radiation, where refractive-index corrections and depth-penetration corrections are relatively small and of opposite sign. Emulsion widths are negligible, but corresponding shifts are significant. Variation with mosaic character is often less than the precision uncertainty.

Integrated reflectivities show expected trends, decreasing with increasing order and being much larger for  $\pi$  than for  $\sigma$  polarization. Perfect-crystal ratios  $|\cos 2\theta|:1$  for  $\sigma:\pi$  reflectivities are most closely observed for infinite-crystal fourth-order calculations, where absorption is minimal. First-order ratios are intermediate between this limit of 0.359:1 and that for ideal mosaicity of  $(\cos 2\theta)^2:1$  or 0.129:1. The first-order ratio is not greatly affected by finite-thickness, curvature or finite-source effects but, over the mosaic-block thickness range from infinity to  $0.5 \mu\text{m}$ , is reduced from 0.266:1 to 0.173:1. Conversely, fourth-order ratios are dramatically affected by the finite lamellar thickness and depth penetration to lie below the ideally imperfect extreme, which is, however, recovered as  $t_0$  reaches  $0.5 \mu\text{m}$ .

These effects are illustrated in Tables 1(d) and (e). First-order reflectivity is doubled over the given range of mosaic-block size, while curvature has little effect (5%). Conversely, curvature is the main contribution for second- and higher-order radiation, which increases fourth-order reflectivity by an order of magnitude and decreases with increasing mosaic character. These results qualify semiempirical modelling. In Table 1(d), estimated computational accuracy is 1 to 2% for  $t_0 < 5 \mu\text{m}$ . The precision of Table 1(e) results is 1% through the use of even steps in the integration coordinate. The two reflectivities differ by about 10% and compare scanning instruments with focusing instruments for finite sources. The reflectivity in the current geometry is the second, larger, figure. This is a separate consideration from any scanning time required and in experiments with

low incident flux it will indicate a preference for the curved-crystal focusing method.

### 7. Comparison with experiment for PET and variation with Bragg angle

Experiments compare hydrogenic iron spectral lines in first-order (Balmer  $\beta$ ,  $\lambda \simeq 7.12 \text{ \AA}$ ) and fourth-order (Lyman  $\alpha$ ,  $\lambda \simeq 1.78 \text{ \AA}$ ) PET 002 diffraction in a Rowland-circle geometry with a finite beam-foil source and photographic detection,  $2Rz = 300 \text{ mm}$ ,  $T = 0.4$  and  $T = 0.1524 \text{ mm}$ , as discussed in paper I and Chantler (1990). Secondary peaks in the detection range include third- fourth- and fifth-order diffraction of Lyman-series radiation, first-order diffraction of the Balmer series and helium-like satellite peaks. This follows earlier work (Silver *et al.*, 1987; McClelland, 1989) in pursuing measurements of QED effects in hydrogenic medium- $Z$  systems such as  $\text{Fe}^{25+}$ .

These peaks yield Doppler-free calibration of the spectrometer geometry subject to correct allowance for diffraction shifts of centroids. They provide estimates of intensities in the source subject to corrections for integrated reflectivities. These two critical parameters are provided in Table 2 for each polarization of given spectral components, together with component identification and values of  $n\lambda$ . Reflectivities and shifts (on the detector  $Y_{iz}$  scale in  $0.1 \mu\text{m}$ ) are given in exponential notation. Theoretical wavelengths and uncertainties of least-significant digits in the rest frame of the beam (*i.e.* without Doppler shifts) are derived following the procedure outlined in Chantler (1990) based on references therein.

The first column numbers resolved components for the observed resolution  $\lambda/\Delta\lambda \sim 2000$ . Mosaic parameters  $t_0 = 0.7 \mu\text{m}$  and  $\eta = 10^{-5}$  rad are discussed in §8. Spectral widths have a significant geometric defocusing component. The calculated minimum of widths *versus* angle agrees with observation, occurring at the pole axis where the crystal lies on the Rowland circle. Complexity of shifts with order and polarization in spectra necessitates accurate calculations of the sort undertaken here. First-order corrections for  $\sigma$ -polarized radiation are larger than for  $\pi$  polarization, as expected from profile asymmetry, but this difference decreases with increasing order. Each order shows a monotonic increase of centroid shift with wavelength; the correction is discussed in paper I, but is the arc around the Rowland circle at the detector relative to kinematic diffraction from the crystal surface and a point source. Perfect-crystal results are given in Chantler (1990).

The slope of the shift *versus*  $n\lambda$  or  $\theta_B$  is almost four times larger for fourth-order than for first-order

Table 1. PET 00(2n) diffraction at  $\lambda = 7.2 \text{ \AA}/n$ ,  $n = 1-4$ ,  $2Rz = 300 \text{ mm}$ ,  $T = 0.4 \text{ mm}$ (a) Contributions to widths on  $\theta_{\text{out}}$  scale,  $10^{-5}$  rad,  $\pm 5 \times 10^{-6}$  rad

Order, polarization	*	1st, $\sigma$	1st, $\pi$	2nd, $\sigma$	2nd, $\pi$	3rd, $\sigma$	3rd, $\pi$	4th, $\sigma$	4th, $\pi$
(-1) Infinite flat perfect (i.f.p.) crystal	1	9.00	24.4	0.67	1.84	0.21	0.60	0.118	0.332
(0) Finite flat perfect (f.f.p.) crystal	2-5	9.11	24.4	2.86	3.07	2.23	2.01	2.11	1.90
(1) Perfect finite flat crystal rocking curve (f.f.c.r.c.) and point source, surface diffraction, focusing/defocusing geometry	5	11.8	29.7	4.16	4.52	3.28	2.31	2.96	2.97
(2) Including depth penetration (many layers)	4	11.8	29.8	12.90	13.7	33.1	33.1	72.2	79.8
(3) Including finite source	3	9.02	26.0	2.78	3.12	2.30	2.30	1.85	1.85
(5) Real perfect curved crystal	-2	9.02	26.0	8.05	7.61	18.7	19.6	44.3	45.9
(6-11) Convolutions with mosaic angular half-width $\eta = 10^{-5}$ rad, block thickness $t_0 = 50 \mu\text{m}$									
(11) = (5) + $10^{-5}$ rad, $50 \mu\text{m}$	-2	9.01	24.7	8.09	8.06	20.3	19.8	44.8	44.9
(12-17) Convolutions with mosaic angular half-width $\eta = 10^{-5}$ rad, block thickness $t_0 = 5 \mu\text{m}$									
(17) = (5) + $10^{-5}$ rad, $5 \mu\text{m}$	-2	16.5	28.5	10.9	11.1	21.1	20.8	44.5	45.6
(23) = (5) + $2 \times 10^{-4}$ rad, $5 \mu\text{m}$	-2	44.6	51.3	42.0	43.7	51.2	48.6	72.8	70.0
(31) = (5) + $10^{-5}$ rad, $0.50 \mu\text{m}$	-2	113.4	133.07	54.27	59.11	42.02	49.34	64.85	55.77†

(b) Perfect-crystal lamellar thicknesses and contributions to FWHM widths on the  $Y_{iz}$  (detector) scale ( $\mu\text{m}$ )

Order, polarization	*	1st, $\sigma$	1st, $\pi$	2nd, $\sigma$	2nd, $\pi$	3rd, $\sigma$	3rd, $\pi$	4th, $\sigma$	4th, $\pi$
Perfect-crystalline thicknesses, $t_0$ ( $\mu\text{m}$ )		59.8	140	10.1	12.2	8.74	9.91	6.69	7.59
(1) Perfect f.f.c.r.c. + Rowland circle	5	27.3	74.9	9.6	10.1	7.5	7.6	6.9	6.5
(2) Including depth penetration, layers	4	27.3	74.9	23.4	23.2	57.9	56.8	125.5	132.3
(3) Including finite source	3	39.6	78.1	33.5	33.1	17.9	19.6	22.0	35.9
(4) Emulsion widths, shifts	-2	0.64	0.64	1.70	1.70	2.82	2.82	3.51	3.51
(5 = 1 + 2 + 3 + 4) finite curved perfect (f.c.p.) crystal	-2	37.3	78.5	40.8	39.3	73.0	73.4	140.9	141.1
(6-11) Convolutions with mosaic angular half-widths $\eta = 10^{-5}$ rad $\rightarrow$ width $\simeq 5.8 \mu\text{m}$ , block thickness $t_0 = 50 \mu\text{m}$									
(11) = (5) + $10^{-5}$ rad, $50 \mu\text{m}$	-2	37.8	78.0	41.0	39.7	73.8	73.7	143.9	143.1
(13) = (1) + $10^{-5}$ rad, $5 \mu\text{m}$	5	48.0	85.0	17.9	19.1	12.7	12.8	10.4	10.4
(17) = (5) + $10^{-5}$ rad, $5 \mu\text{m}$	-2	51.8	85.8	43.7	44.6	73.3	74.7	145.2	145.2
(27) = (5) + $10^{-5}$ rad, $0.7 \mu\text{m}$	-2	244.1	288.7	123.4	117.9	119.5	105.2	179.8	175.0
(27b) = (5) + $10^{-5}$ rad, $0.7 \mu\text{m}\ddagger$	-2	248.1	286.6	127.7	103.6	104.6	90.0	102.9	102.0
(28) = (5) + $5 \times 10^{-5}$ rad, $0.7 \mu\text{m}$	-2	244.1	295.5	127.7	118.7	125.5	106.8	183.3	180.7
(31) = (5) + $10^{-5}$ rad, $0.5 \mu\text{m}$	-2	334.6	371.6	160.7	178.4	129.9	149.0	196.2	176.5†

(c) Shifts on detector scale (to larger Bragg angles, longer  $Y_{iz}$  arcs) for  $2Rz = 300 \text{ mm}$  PET 00(2n) diffraction at  $\lambda = 7.2 \text{ \AA}/n$ ,  $n = 1-4$ ,  $T = 0.4 \text{ mm}$ ,  $\pi$  and  $\sigma$  polarizations ( $\mu\text{m}$ )

Order, polarization	1st, $\sigma$	1st, $\pi$	2nd, $\sigma$	2nd, $\pi$	3rd, $\sigma$	3rd, $\pi$	4th, $\sigma$	4th, $\pi$
(-1) From i.f.p. crystal $\Delta\theta$ rad	69.86	68.13	17.48	17.48	7.72	7.74	4.33	4.33
(1) Perfect f.f.c.r.c. + Rowland circle	68.33	66.20	15.08	14.84	5.66	5.36	2.73	2.46
(2) Including depth penetration, layers	68.33	66.20	-1.41	-0.98	-52.18	-52.28	-94.50	-94.72
(3) Including finite source	64.57	61.26	13.56	12.54	2.38	3.90	-4.36	-1.06
(4) Emulsion shifts	0.64	0.64	1.70	1.70	2.82	2.82	3.51	3.51
(5 = 1 + 2 + 3 + 4) f.c.p. crystal	65.07	61.65	-2.06	-2.00	-52.46	-51.59	-91.73	-91.70
(17) = (5) + $10^{-5}$ rad, $5 \mu\text{m}$	67.71	59.09	-2.96	-1.54	-51.80	-52.88	-91.02	-90.97
(25) = (5) + $10^{-5}$ rad, $0.75 \mu\text{m}$	65.06	58.82	-1.75	-1.02	-51.46	-50.70	-90.40	-89.59
(26) = (5) + $10^{-5}$ rad, $0.75 \mu\text{m}$	65.1	59.14	-2.2	-1.8	-52.1	-51.7	-90.3	-90.35
(27) = (5) + $10^{-5}$ rad, $0.7 \mu\text{m}$	63.15	57.53	-2.00	-1.39	-52.08	-50.91	-90.23	-90.59
(27b) = (5) + $10^{-5}$ rad, $0.7 \mu\text{m}\ddagger$	63.03	56.65	-2.421	-2.792	-28.68	-28.71	-37.85	-37.73
(28) = (5) + $5 \times 10^{-5}$ rad, $0.7 \mu\text{m}$	63.33	57.36	-1.98	-1.51	-52.03	-50.88	-90.07	-89.29
(31) = (5) + $10^{-5}$ rad, $0.5 \mu\text{m}$	64.11	57.78	-2.47	-2.71	-51.97	-51.80	-90.51	-89.81

radiation, of order  $55 \mu\text{m} \text{ \AA}^{-1}$  or  $290 \mu\text{m} \text{ rad}^{-1}$ . The curvature of this relation is large for both orders, but of opposite sign. For first-order radiation, this is dominated by the refractive-index correction

$$\Delta\lambda/\lambda \simeq -[2d/(n\lambda)]^2 \delta \simeq -2 \times 10^{-6} (2d/n)^2 \text{ \AA}^{-2} \quad (10)$$

corresponding to neglect of profile asymmetry with

$\delta \propto \psi'_0 \propto \lambda^2$ . The shift due to profile asymmetry for  $\pi$  polarization corresponds to  $-dy$  with  $0 < dy < \Delta y_0/2$ . Equation (10) gives

$$\Delta Y_{iz} \simeq 2Rz \Delta\theta_{\text{out}} \propto \tan \theta_B. \quad (11)$$

Refractive-index shifts scale with order  $n$  as  $n^{-2}$ . Dominant contributions to the fourth-order shift

Table 1 (cont.)

(d) Integrated reflectivity  $R_{H^0}^{0^*} = \int (P_H/P_0)d\theta_{inc}$  (rad) for comparison with flat crystal  $R_C$ , exponential notation. Estimated uncertainty =  $\pm 1$ -2% [line (28)  $\pm 3\%$ ]; nc: not calculated

Order, polarization	1st, $\sigma$	1st, $\pi$	2nd, $\sigma$	2nd, $\pi$	3rd, $\sigma$	3rd, $\pi$	4th, $\sigma$	4th, $\pi$
(-1) Infinite flat perfect $R_C$	6.57E-5	2.47E-4	5.10E-6	1.86E-5	1.95E-6	6.57E-6	1.23E-6	3.84E-6
(0) Perfect f.f.c.r.c. $R_C$	6.59E-5	2.54E-4	2.47E-6	1.79E-5	3.61E-7	3.25E-6	1.13E-7	1.00E-6
(1) Perfect f.f.c.r.c. + Rowland circle	6.35E-5	2.50E-4	2.39E-6	1.79E-5	3.80E-7	3.18E-6	1.19E-7	1.08E-6
(2) Including depth penetration	6.35E-5	2.50E-4	8.82E-6	5.11E-5	4.71E-6	3.39E-5	3.72E-6	3.00E-5
(3) Including finite source	6.78E-5	2.62E-4	2.49E-6	1.86E-5	3.99E-7	3.33E-6	1.25E-7	1.14E-6
(5) Real perfect curved crystal	6.78E-5	2.62E-4	8.98E-6	5.22E-5	4.77E-6	3.42E-5	3.73E-6	3.00E-5
(11) = (5) + $10^{-5}$ rad, 50 $\mu\text{m}$	6.78E-5	2.62E-4	9.09E-6	5.18E-5	4.67E-6	3.42E-5	3.79E-6	2.84E-5
(12-17) Convolutions with mosaic angular half-width $\eta = 10^{-5}$ rad, block thickness $t_0 = 5 \mu\text{m}$								
(12) = 0 + $10^{-5}$ rad, 5 $\mu\text{m}$	6.20E-5	2.71E-4	1.30E-6	9.75E-6	2.23E-7	1.70E-6	9.10E-8	7.08E-7
(13) = (1) + $10^{-5}$ rad, 5 $\mu\text{m}$	5.87E-5	2.57E-4	1.29E-6	9.39E-6	2.17E-7	1.67E-6	8.71E-8	6.91E-7
(17) = (5) + $10^{-5}$ rad, 5 $\mu\text{m}$	8.21E-5	3.10E-4	9.23E-6	5.81E-5	4.81E-6	3.47E-5	3.92E-6	2.95E-5
(23) = (5) + $2 \times 10^{-4}$ rad, 5 $\mu\text{m}$	8.94E-5	3.43E-4	8.87E-6	6.23E-5	4.69E-6	3.23E-5	3.85E-6	2.78E-5
(28) = (5) + $10^{-5}$ rad, 0.7 $\mu\text{m}\ddagger$	1.03E-4	5.55E-4	8.89E-6	5.21E-5	4.57E-6	2.66E-5	3.64E-6	2.71E-5
(30a) = (0) + $10^{-5}$ rad, 0.6 $\mu\text{m}$ , f.f.c.r.c.	1.47E-5	1.14E-4	nc	nc	nc	nc	1.11E-8	8.73E-8
(30) = (5) + $10^{-5}$ rad, 0.6 $\mu\text{m}$	9.76E-5	5.77E-4	nc	nc	nc	nc	3.66E-6	2.80E-5
(31) = (5) + $10^{-5}$ rad, 0.5 $\mu\text{m}$	1.04E-4	6.01E-4	7.62E-6	6.50E-5	3.71E-6	3.48E-5	3.56E-6	2.31E-5

(e) Integrated reflectivity  $R_H^0 = \int (P_H/P_0)d\theta_S = 2\pi I_{out}/I_0$  for  $I_0$  photons in  $2\pi$  rad, exponential notation

Order, polarization	1st, $\sigma$	1st, $\pi$	2nd, $\sigma$	2nd, $\pi$	3rd, $\sigma$	3rd, $\pi$	4th, $\sigma$	4th, $\pi$
(1) Perfect f.f.c.r.c. + Rowland circle	6.90E-5	2.71E-4	2.60E-6	1.94E-5	4.13E-7	3.45E-6	1.29E-7	1.17E-6
(2) Including depth penetration	6.90E-5	2.71E-4	9.55E-6	5.55E-5	5.11E-6	3.68E-5	4.04E-6	3.25E-5
(3) Including finite source	7.35E-5	2.84E-4	2.70E-6	2.02E-5	4.33E-7	3.61E-6	1.36E-7	1.24E-6
(5) Real perfect curved crystal	7.36E-5	2.84E-4	9.75E-6	5.66E-5	5.17E-6	3.71E-5	4.04E-6	3.25E-5
(11) = (5) + $10^{-5}$ rad, 50 $\mu\text{m}$	7.36E-5	2.84E-4	9.86E-6	5.62E-5	5.06E-6	3.71E-5	4.11E-6	3.09E-5
(13) = (1) + $10^{-5}$ rad, 5 $\mu\text{m}$	6.64E-5	2.80E-4	1.41E-6	1.05E-5	2.38E-7	1.83E-6	9.76E-8	7.58E-7
(17) = (5) + $10^{-5}$ rad, 5 $\mu\text{m}$	8.91E-5	3.36E-4	1.00E-5	6.31E-5	5.22E-6	3.77E-5	4.25E-6	3.20E-5
(27) = (5) + $10^{-5}$ rad, 0.7 $\mu\text{m}$	1.11E-4	6.01E-4	9.65E-6	5.74E-5	4.96E-6	2.99E-5	3.95E-6	2.94E-5
(27b) = (5) + $10^{-5}$ rad, 0.7 $\mu\text{m}\ddagger$	1.10E-4	6.01E-4	9.35E-6	5.07E-5	3.87E-6	2.10E-5	2.24E-6	1.65E-5
(28) = (5) + $5 \times 10^{-5}$ rad, 0.7 $\mu\text{m}$	1.11E-4	6.02E-4	9.65E-6	5.66E-5	4.96E-6	2.89E-5	3.95E-6	2.94E-5
(31) = (5) + $10^{-5}$ rad, 0.5 $\mu\text{m}$	1.12E-4	6.52E-4	8.27E-6	7.05E-5	4.03E-6	3.77E-5	3.87E-6	2.51E-5

\* Control parameter indicating test.

† Erroneous due to finite precision.

‡ Calculation for crystal thickness  $T = 0.1524$  mm.

dependence on Bragg angle arise from decreasing effective crystal thickness and varying mean depth of penetration with angle. To first order, this is due to the variation of mean grazing incidence angle at the surface compared with the Bragg angle at the diffracting planes. With the absorption coefficient  $\mu$ , this is given approximately by

$$\Delta\theta_{out} \simeq -[\bar{d}/(2Rz)] \cot \theta_B,$$

$$\bar{d} \simeq \begin{cases} T/2, & T \ll 1/\mu; \\ (1/2\mu) \sin \theta_B \propto (\sin \theta_B)^{-1.9}, & T \gg 1/\mu. \end{cases} \quad (12)$$

For thin crystals or high-order radiation, the former case is appropriate and larger, corresponding to a  $-200 \mu\text{m}$  shift on the detector scale, as observed. Secondary components include corrections for the above, in addition to a shift of the exit location of the ray owing to depth penetration (secondary variables

are defined in paper I):

$$\Delta Y_{iz} \simeq -\cot \theta_{out} [(\sin \theta_A)/2] XZ, \quad XZ \simeq 2\bar{d} \cot \theta_B,$$

$$\sin \theta_A = \max[XXz/(2Rz), XZ/(2Rz)]. \quad (13)$$

Calculated shifts agree well with the sum of these estimates, reproducing the dependence on  $\theta_B$ . Further agreement of shifts and reflectivities with experiment will be discussed briefly below, but may be taken as verified at the 10% level (Chantler, 1990). Additional powerful tests of theory and modelling are provided by widths and profiles.

## 8. Convolutions, fitting errors and interpretation of widths

Observed widths and profiles involve convolution of above calculations with a known slit broadening from

Table 2. *One- and two-electron Fe X-ray wavelengths and uncertainties in Å*

Effect of Doppler shifts  $\Delta\lambda = \lambda_D - \lambda_{\text{rest}}$  included with diffraction shifts (on  $Y_{iz}$  scale, 0.1  $\mu\text{m}$ ) and integrated reflectivities (on  $\theta_s$  scale). Imperfect PET 00(2n) crystal,  $T = 0.4$  mm,  $2Rz = 300$  mm. Resolution = 2000, source FWHM = 20 mm,  $\beta = 0.136$ ,  $t_0 = 0.70$   $\mu\text{m}$ ,  $\eta = 10^{-5}$  rad.

Line	$n\lambda_{\text{rest}}$ (Å)	$\sigma$	$R_{\text{H}}^{\text{a}}$		$Y_{iz}-Y_{oz}$ shift		Description	Order $n$
			$\pi$	$\sigma$	$\pi$	$\sigma$		
1	5.3340487 (18)	2.157E-06	2.050E-05	-1.645E+03	-1.636E+03	Ly $\alpha$ 1s1/2-2p3/2	3	
2	5.3454819 (20)	1.356E-06	2.308E-05	-2.123E+03	-2.123E+03	Series limit, 1s1/2-	4	
3	5.3503261 (18)	2.081E-06	2.390E-05	-1.628E+03	-1.613E+03	Ly $\alpha$ 1s1/2-2p1/2	3	
4	5.3800764 (71)	4.206E-05	4.757E-04	2.963E+02	2.532E+02	Series limit, 2p3/2-	1	
5	5.4560905 (100)	1.018E-06	2.366E-05	-2.018E+03	-2.014E+03	Ly $\zeta$ 1s1/2-7p3/2	4	
6	5.4972019 (100)	9.061E-07	2.379E-05	-1.982E+03	-1.978E+03	Ly $\epsilon$ 1s1/2-6p3/2	4	
7	5.5508547 (120)	2.646E-05	4.783E-04	3.096E+02	2.770E+02	Ba $\delta$ 2p1/2-10d3/2	1	
8	5.5667830 (20)	7.414E-07	2.394E-05	-1.923E+03	-1.917E-03	Ly $\delta$ 1s1/2-5p3/2	4	
9	5.5785470 (48)	1.028E-06	2.396E-05	-1.426E+03	-1.414E+03	1s2 1S0-1s2p 3P1	3	
10	5.6051159 (1120)	1.805E-05	4.793E-04	3.168E+02	2.849E+02	Ba $\gamma$ 2p1/2-9d3/2	1	
12	5.6827922 (120)	1.592E-05	4.811E-04	3.268E+02	2.959E+02	Ba $\zeta$ 1s1/2-8d3/2	1	
13	5.6886193 (22)	4.393E-07	2.330E-05	-1.811E+03	-1.791E+03	Ly $\gamma$ 1s1/2-4p3/2	4	
15	5.8000550 (124)	8.814E-06	4.845E-04	3.618E+02	3.125E+02	Ba $\epsilon$ 2p1/2-7d3/2	1	
16	5.8595185 (86)	5.093E-06	4.890E-04	3.572E+02	3.218E+02	Ba $\epsilon$ 2p3/2-7s1/2	1	
17	5.9905567 (130)	1.286E+06	4.937E-04	3.776E+02	3.417E+02	Ba $\delta$ 2p1/2-6d3/2	1	
18	6.0094018 (24)	3.354E-08	2.493E-05	-1.578E+03	-1.576E+03	Ly $\beta$ 1s1/2-3p3/2	4	
20	6.0548453 (92)	3.211E-07	4.940E-04	3.840E+02	3.548E+02	Ba $\delta$ 2p3/2-6s1/2	1	
21	6.2926970 (56)	8.974E-08	2.469E-05	-1.388E+03	-1.381E+03	1s2 1S0-1s3p 1P1	4	
24	6.3357635 (100)	3.605E-06	5.142E-04	4.092E+02	3.997E+02	Ba $\gamma$ 2p1/2-8d3/2	1	
26	6.4095569 (103)	7.940E-06	5.154E-04	4.679E+02	4.026E+02	Ba $\gamma$ 2p3/2-5s1/2	1	
27	6.7026525 (260)	3.385E-05	5.421E-04	5.212E+02	4.601E+02	1s2s 3S1-1s5p 3P2	1	
36	6.9460845 (260)	6.700E-05	5.750E-04	5.557E+02	5.173E+02	1s2p 1P1-1s5s 1S0	1	
37	6.9584785 (25)	8.912E-07	1.011E-05	-1.177E+03	-1.177E+03	Ly $\delta$ 1s1/2-5p3/2	5	
38	7.0878077 (126)	9.500E-05	5.952E-04	6.090E+02	5.545E+02	Ba $\beta$ 2p1/2-4d3/2	1	
39	7.1005354 (126)	9.782E-05	5.972E-04	6.080E+02	5.582E+02	Ba $\beta$ 2s1/2-4p1/2	1	
40	7.1120653 (24)	3.828E-06	2.868E-05	-9.183E+02	-9.133E+02	Ly $\alpha$ 1s1/2-2p3/2	4	
41	7.1245241 (27)	1.382E-06	1.062E-05	-1.085E-03	-1.085E+03	Ly $\gamma$ 1s1/2-4p3/2	5	
42	7.1337681 (24)	3.917E-06	2.883E-05	-9.072E+02	-9020E+02	Ly $\alpha$ 1s1/2-2p1/2	4	
43	7.1712089 (129)	1.198E-04	6.086E-04	6.450E+02	5.786E+02	Ba $\beta$ 2p3/2-4d5/2	1	
45	7.1855149 (129)	1.235E+04	6.111E-04	6.494E-02	5.828E+02	Ba $\beta$ 2p3/2-4s1/2	1	
46	7.4015937 (56)	7.088E-06	3.093E-05	-7.661E+02	-7.643E+02	1s2 1S0-1s2p 1P1	4	
50	7.4922247 (8400)	2.131E-04	6.728E-04	7.167E+02	6.908E+02	1s2s 3S1-1s4p 3P0	1	
58	7.7920461 (1680)	3.574E-04	7.655E-04	8.910E+02	8.427E+02	1s2p 1P1-1s4s 1S0	1	

densitometry (typically 170  $\mu\text{m}$ ) and an additional divergence or defocusing width. Forward scattering off a polypropylene crystal window and aluminium-coated Mylar film windows gives a negligible background. A densitometer angle of 0.052 rad increases widths by 0.14% or 0.5  $\mu\text{m}$  and is insignificant. Parameters of polarization, mosaic-block size and angular half-width are initially unknown, as with other models.

Two-dimensional data are obtained on numerous lines, so that a series of one-dimensional scans of the Lyman  $\alpha$ -Balmer  $\beta$  region minimizes statistical uncertainty of widths and profiles. Nine scans were fitted by least-squares techniques with Voigt profiles (or Lorentzians convolved with slits) with two independent width parameters (Chantler, 1990). Each pair of Lyman peaks has a constant width profile and the seven Balmer components are assumed to have a separate but constant width profile. This follows from the energy dependence of profiles and the narrow angular range involved and is observed in the data.

Each fit therefore involves four width parameters. Voigt profiles provide superior fits (Fig. 4). Analysis of a given test film led to final widths of  $w_T = (w_L^2 + w_C^2)^{1/2} = 330$  (15)  $\mu\text{m}$  for first-order (Balmer  $\beta$ ) radiation and  $w_T = 252$  (15)  $\mu\text{m}$  for fourth-order (Lyman  $\alpha$ ) radiation (Table 3). The scatter directly affects the estimated block thickness with little effect on shifts. Errors depend slightly on the fitting range. Noise is assumed statistical, with negligible error. For further details, see Chantler, Laming, Silver, Dietrich & Hallett (1992).

PET crystals are soft and deform plastically, implying that flat and curved crystals have mosaic behaviour. A first estimate of 5  $\mu\text{m}$  for the mosaic-block thickness limits the mosaic angular half-width to less than  $3 \times 10^{-4}$  rad (neglecting other broadening effects). Agreement with fourth-order Lyman  $\alpha$  experimental widths after inclusion of the known 170  $\mu\text{m}$  slit width and a presumed 80  $\mu\text{m}$  Doppler/defocusing width requires that this half-width be less than  $1.5 \times 10^{-4}$  rad. This neglects

Table 3. Results for  $2Rz = 300$  mm PET 00(2n) diffraction at  $\lambda = 7.2 \text{ \AA}/n$ ,  $n = 1, 4, \pi$  and  $\sigma$  polarizations(a) Contributions to widths on  $Y_{iz}$  detector scale ( $\mu\text{m}$ )

Order, polarization	1st, $\sigma$	1st, $\pi$	4th, $\sigma$	4th, $\pi$
Known contributions				
(32) 1 mm slit width with grid wires yields 193 (max.), 170 (mean), 157 (min.) $\mu\text{m}$ slit broadening				
(32a) Natural widths (Lorentzians)	$4p = 7.08; 4d = 2.42;$ $4s = 0.38$		$2p = 11.9$	$2p = 11.9$
Convolutions: overall widths [FWHM, cf. Table 1(b)]				
(33) $28 + 32 + G(130 \mu\text{m})$ convolution	317.9	327 (5)	287.4	269 (5)
(33a) $28 + 32 + G(200 \mu\text{m})$ convolution	340.4	363 (5)	323.9	312 (5)
(33c) $30 + 32 + G(135 \mu\text{m})$ convolution	337.1	380 (5)	276.1	277 (5)
(33d) $30 + 32 + L(100 \mu\text{m})$ convolution	370.2	402.5 (50)	304.7	307.0 (50)
Convolutions: $w_T$ values from Voigt fits				
(34) $w_T$ , Voigt fit of (33), $0.70 \mu\text{m}$	263	272 (1)	249	235 (1)
(34a) $w_T$ for (33a), $0.70 \mu\text{m}$	293	323 (2)	274	281 (1)
(34b) $w_T$ for $29 + 32 + G(140 \mu\text{m})$ , $0.65 \mu\text{m}$	276	289 (2)	242	243 (2)
(34c) $w_T$ for (33c), $0.60 \mu\text{m}$	288.9	320.6 (12)	238.4	253.8 (14)
(34d) $w_T$ for (33d), $0.60 \mu\text{m}$	319.7	323.8 (10)	255.2	252.1 (10)
Experiment				
(35) $w_T$ , A120M( $\Delta\alpha_{\beta m}$ and defocusing)		330 (15)		252 (15)
(36) $\{[40]^2 - [32]_L^2 - [32]_S^2\}^{1/2}$ [cf. $0.7 \mu\text{m}$ , row (28)]		283 (18)		186 (21)

(b) Shifts (to larger Bragg angles, longer  $Y_{iz}$  arcs,  $\mu\text{m}$ ) ( $\pm 0.45 \mu\text{m}$ )

Order, polarization	1st, $\sigma$	1st, $\pi$	4th, $\sigma$	4th, $\pi$
(34) Voigt fit, $0.70 \mu\text{m} +$ convolution	63.15	57.53	-88.16	-88.28
(34b) Voigt fit, $0.65 \mu\text{m} +$ convolution	63.35	58.21	-88.76	-88.52
(34c) Voigt fit, $0.60 \mu\text{m} + G/S$	64.14	57.39	-88.69	-88.95
(34d) Voigt fit, $0.60 \mu\text{m} + L/S$	64.14	57.39	-89.09	-89.06

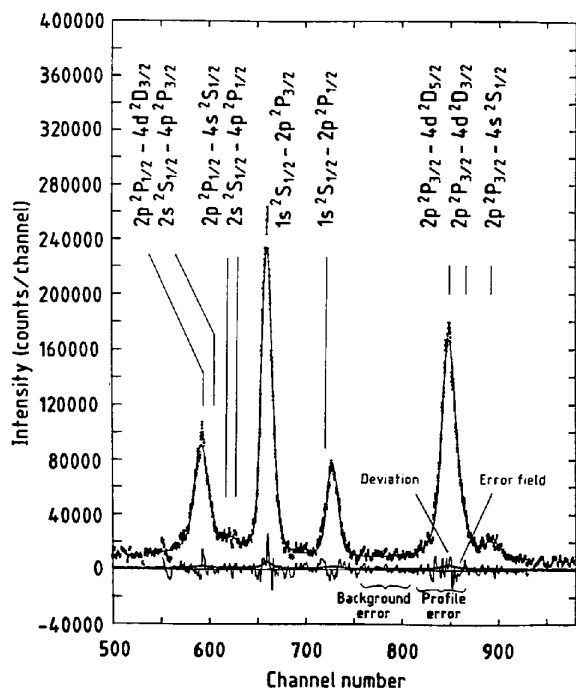


Fig. 4. Fit of Lyman  $\alpha$ -Balmer  $\beta$  region for one scan of film A120 using Voigt profiles with four free width parameters, four free parameters defining centroid location and nine free intensities.  $\chi^2 = 6.0$  (dominated by profile inadequacy).

first-order widths, which are larger than fourth-order values. This is incompatible with a block thickness larger than  $1 \mu\text{m}$  [see Tables 1(a) and (b)].

Defocusing from the crystal, being off the Rowland circle, is symmetric and depends on the diffracting angle (and hence on the  $2d$  spacing). Divergence and Doppler widths depend on accelerator conditions but are symmetric. The only widths not equal for first- and fourth-order radiation are natural linewidths (with possible Stark broadening) and diffraction/focusing profile widths in Table 1(b). The widths therefore specify precisely the degree of order asymmetry.

Agreement of model and experiment for this asymmetry can only be obtained for  $0.7 > t_0 > 0.55 \mu\text{m}$ . Below this, first-order radiation is too wide, even allowing for the uncertainty and neglecting Doppler and defocusing widths. Above this, the first-order width is too narrow compared with fourth-order widths. Polarization shifts of  $6 \mu\text{m}$  broaden first-order radiation negligibly and only if the ratio of emitted  $\sigma:\pi$  radiation is 10:1 (owing to reflectivity ratios).

Broadening by the densitometry slit height and estimated  $40 \mu\text{m}$  Doppler/defocusing widths yields  $\eta < 8 \times 10^{-5}$  rad. First-order radiation is affected little by  $\eta$ , but broadening is significant for

fourth-order profiles. Summation in quadrature of experimental widths leads to row (36) of Table 3, corresponding to a  $0.7\ \mu\text{m}$  block thickness for  $\pi$ -polarized radiation. Calculations were performed for this case with  $\eta = 5 \times 10^{-5}$  rad.

These profiles are convolved with natural line widths (Lorentzian), the slit width (top-hat function) and symmetric Doppler, defocusing and mosaic angular broadening, initially assumed to be Gaussian in character. The result is assumed Voigt like for experimental centroid analysis. Gaussian widths add in quadrature, but not slit or other widths; and Voigt fits will not yield accurate widths for odd profiles. To allow for this, a convolution program added known widths to output diffraction profiles. A package *GENEXN* fitted these after scaling and adding a typical background (Chantler, 1990).

This regime [row (33) of Table 3,  $0.7\ \mu\text{m}$ ,  $5 \times 10^{-5}$  rad, with broadening widths of  $130\ \mu\text{m}$ ] yields convolved widths slightly larger than experimental values of  $w_T$ . The width parameter  $w_T$  is however 15 and 10% less than the real total width for first- and fourth-order radiation, respectively.  $w_T$  is the parameter from Voigt fits, so agreement with this is necessary and is only gained for the regime  $0.6\ \mu\text{m}$ ,  $1 \times 10^{-5}$  rad with a Gaussian Doppler/defocusing width of  $135\ \mu\text{m}$  [row (34c)]. This yields fitted width ratios of  $w_G/w_T = 0.98$  (1) and  $0.99$  (1) for first- and fourth-order radiation, respectively.

Assumption of defocusing with a Lorentzian profile does not affect the block thickness, but requires only a  $100\ \mu\text{m}$  broadening to achieve the same widths. Lorentzian fits yield  $w_G/w_T = 0.85$  (1),  $0.90$  (1), reproducing observed values of  $w_G/w_T = 0.81$  (2),  $0.92$  (2) for first- and fourth-order lines. Additional broadening contributions are thus near-Lorentzian in profile. The possibility of significant Voigt-fitting width errors from unresolved Balmer components or noise is eliminated by observed fits to the data, especially at peaks.

Pure  $\sigma$  polarization would also yield  $t_0 \simeq 0.60\ \mu\text{m}$ . Profile FWHM values for first-order  $\sigma$  radiation (with or without convolution) are  $30$  to  $55\ \mu\text{m}$  (14%) less than corresponding  $\pi$ -polarized radiation, but the profile shape and variation in  $w_G/w_T$  lead to the same values for  $w_T$  and  $t_0$ . However, the width ratios  $w_G/w_T = 0.97, 0.93$  are not in agreement with the data, even for the Lorentzian broadening extreme. This implies that  $\pi$ -polarized radiation is dominant. Tests with  $(\sigma:\pi)_{\text{out}} = 1:1$  and  $1:6$  show smooth variation of  $w_T$  and  $w_G/w_T$  between these extremes, confirming the optimum block width and implying that the incident beam is partially  $\pi$  polarized leading to pure  $\pi$  radiation in the diffracted beam with an uncertainty of less than 10%. The Lyman polarization is not defined since major polarization and profile effects apply to first-order radiation.

## 9. The test of theory, additional data and symmetry of profiles

The ability to fit block widths, broadening widths and profiles from experimental data to within narrow limits restricts model-dependent uncertainties in shifts and reflectivities. Success of fits for  $w_T$  and  $w_G/w_T$  for first and fourth orders is a good test of diffraction theory and computation. If experimental width ratios  $w_G/w_T$  were lower than 0.75 or if the width difference between orders,  $w_T|_{1\text{st}} - w_T|_{4\text{th}}$ , was 50% greater with the same Lyman  $\alpha$  width  $w_T|_{4\text{th}}$ , no agreement of model and experiment would be possible given any broadening profile. Equally, a Balmer width  $w_T|_{1\text{st}}$  less than 0.84 of this Lyman width or a Lyman width of less than 0.70 of the experimental value would not agree with theory (unless the crystal thickness varied outside tolerance limits).

Comparison of scans with different slit widths with calculated profiles and convolutions confirms these parameters. Comparison of widths of peaks around the Rowland circle gives an estimate of defocusing (relative to minimum widths at the pole axis of the crystal, near Balmer  $\epsilon$  peaks). This width dependence agrees with ideal (computed) defocusing to better than 10% and implies that additional defocusing aberrations are negligible for this experiment. An additional broadening mechanism is due to beam divergence (the source distribution has already been included and variation in beam velocity due to the accelerator or to straggling in the target is negligible). The value of the divergence extracted is therefore limited by the width data and agrees with other estimates. Increased broadening due to straggling is observed with thick targets at the expected level.

The model neglects mosaic sizes of other than the mean value  $t_0$  and assumes that angular distributions are Gaussian. The latter yields a low value for the angular width, whereas use of a Lorentzian profile would allow angular widths 2 to 3 times larger to fit the data. Divergence estimates would then be lower than expected.

Despite asymmetries and secondary peaks in diffraction profiles, convolved fourth-order profiles in Fig. 5 are smooth and near-symmetric, with centroids accurately fitted by the finite-precision Voigt-fitting routine. However, shifts (between centroid locations and results of Voigt fitting) remain significant. Fitting uncertainties include noise, unresolved components and variations in background and statistics.

Conversely, profiles of Lyman  $\alpha$  in third order are not symmetric after convolving with the known slit width (approximately  $115\ \mu\text{m}$ ) and an assumed Lorentzian defocusing width identical to the fourth-order value of  $100\ \mu\text{m}$ . Fig. 6 displays the inadequacy of Voigt (or any symmetric function) fitting of these lines. The fit still provides estimates of the centroids

of these secondary calibration lines with an error of only 12  $\mu\text{m}$ . This accuracy is good. The correct shift is imprecise due to the use of a  $t_0 = 0.7 \mu\text{m}$  calculation, with unknown (Lorentzian) broadening, but qualitative agreement of observed and convolved profiles and of their goodness-of-fits is excellent.

An earlier calculation (McClelland, 1989) for hydrogenic iron radiation and PET quotes  $R_C = 1.8 \times 10^{-4}$  and  $1.1 \times 10^{-5}$  for first- and fourth-order ( $\pi$ ) radiation for an infinite flat perfect crystal (Burek, 1976). Associated interpolation and calculation errors were 27 and 65% for the two orders. Estimated profiles and shifts for a point source, the Rowland-circle geometry and explicit 2.3 mrad divergence led to enormous reflectivities ( $9.9 \times 10^{-3}$  and  $2.3 \times 10^{-4}$ , factors of 20 and 9 too large, respectively). The overestimate resulted from use of infinite flat crystal rocking curves assuming that the diffracting angle is constant with depth, leading to infinite coherence lengths. Rocking-curve profiles and angular shifts are in agreement with the current calculation. Further details are given elsewhere (Chantler, 1990).

#### 10. Effects of errors in crystal and spectrometer parameters: PET 002

Determination of mosaic parameters is incomplete without uncertainties, which depend on tolerances of alignment and crystal parameters. Uncertainties and systematic errors on the  $Y_{iz}$  (film) scale for the first- to fourth-order shifts are given in Table 4. Large

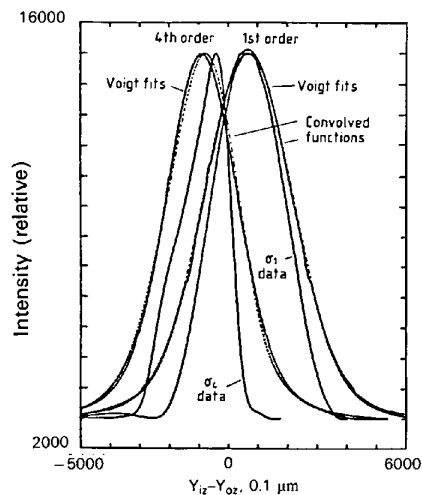


Fig. 5. Profiles for PET 00(2n) finite curved imperfect crystal diffraction at  $7.2 \text{ \AA}/n$ ,  $n = 1, 4$ ,  $\sigma$ -polarized radiation, convolved by  $170 \mu\text{m}$  slit and  $100 \mu\text{m}$  Lorentzian defocusing broadening and fitted by Voigt profiles.  $T = 0.4 \text{ mm}$ ,  $t_0 = 0.7 \mu\text{m}$  and  $\eta = 5 \times 10^{-5}$  rad. Unconvolved diffraction profiles are highly asymmetric and many peaked, but convolved functions are smooth and near-symmetric, with centroids fitted to high accuracy by finite-precision Voigt fitting routines.

absolute uncertainties relating to the location of lines on the film correspond to negligible differential shifts for first or fourth orders and to negligible first- to fourth-order corrections.

Uncertainties in the beam velocity, angle and polarization contribute at the submicrometre level; contributions from the mosaic-block thickness and angular width are two orders of magnitude less! Error in the original crystal curvature is negligible, as proven by interferometry, but may arise from allowance for the bending-post width (leading to  $Cx \pm 0.03 \text{ mm}$ ) and from possible relaxation of crystals during experiments (modifying  $Cx$  and  $2Rz$ ).

Test results show that the parameters are shifted by the quoted standard deviations.  $2d$  and atomic sites are well defined and imprecision of thermal parameters is negligible. Form factors are generally accurate to 2 or 5% within  $\Delta E/E < 20\%$  of an absorption edge or above 10 keV. Form factors and O-atom coordinates are asymmetrically shifted by their uncertainty to yield unaltered shifts and reflectivities. Effects due to  $T$ ,  $\alpha_{\text{plane}}$ ,  $2Rz$ ,  $Rzf$  and  $Cx$  on width uncertainties can be treated as 'defocusing' broadening. These uncertainties do not impair the precise constraint on mosaic parameters [Table 4(c)].

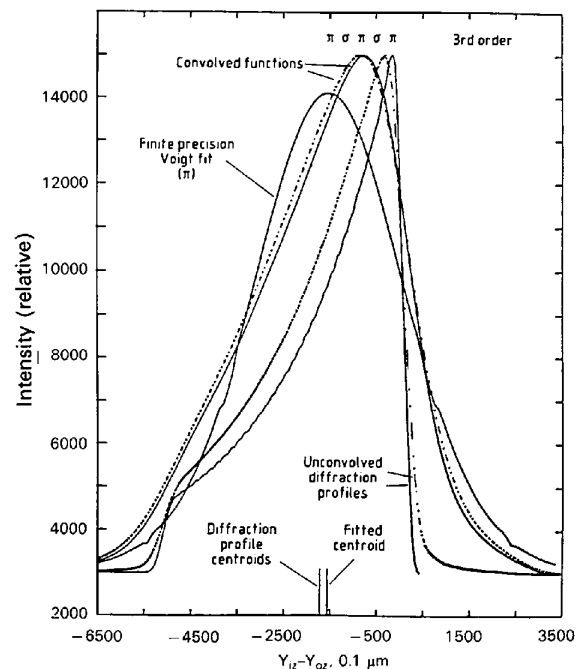


Fig. 6. Profiles for PET 006 finite curved imperfect crystal diffraction for Lyman  $\alpha$  radiation, convolved by  $115.3 \mu\text{m}$  slit and assumed  $100 \mu\text{m}$  Lorentzian defocusing broadening, and fitted by Voigt profiles.  $T = 0.4 \text{ mm}$ ,  $t_0 = 0.7 \mu\text{m}$  and  $\eta = 5 \times 10^{-5}$  rad. Unlike Fig. 5, convolved functions remain markedly asymmetric and are not well fitted by Voigt functions. Convolved profiles agree qualitatively with experiment in both cases, as does the degree of goodness-of-fit.

Table 4. Results for Lyman  $\alpha$ -Balmer  $\beta$  region for PET 00(2n) diffraction,  $2Rz = 300$  mm at  $\lambda = 7.2 \text{ \AA}/n$ ,  $n = 1, 4, \pi$  and  $\sigma$  polarizations

Scaling:  $(\Delta\lambda/\lambda)/\Delta Y_{iz} = (2.32 \times 10^{-6}; 2.21 \times 10^{-6}) \mu\text{m}^{-1}$  (Ba  $\beta_{1-4}$ ; Ba  $\beta_{5-7}$ ).

(a) Summary of uncertainties and errors ( $\mu\text{m}$ )

Uncertainties in shifts are due to the finite precision of calculations. Variables with negligible effects (see paper I):  $BDz = 15$  (1) mm,  $BXz = 26$  (1) mm, Gaussian source FWHM = 20 (2) mm. Densitometry: Heidenhain angle  $\alpha' = 0.050$  (5) rad, step parameter  $Ns$  scale = 0.00 (2), crystal length = 24 (2) mm, longitudinal and transverse drive angles  $\alpha'' = 0.000$  (5) rad,  $\alpha'_2 = 0.00$  (2) rad, step length = 20.0 (4)  $\mu\text{m}$  per channel

Order, polarization	Value (Uncertainty)	1st, $\pi$ $Y_{iz}$ shift (Absolute)	4th, $\pi$	1st, $\pi$ $Y_{iz}-Y_{oz}$ shift (Differential)	4th, $\pi$	4th-1st, $\sigma$ $Y_{iz}-Y_{iz}$ shift (Relative)	4th-1st, $\pi$
With respect to 0.7 $\mu\text{m}$ values		290577	290493	57.53	-90.59	-153.38	-148.12
Versus 0.6 $\mu\text{m}$ calculation		290603	290488	57.39	-90.28	-154.29	-147.67
High-precision 0.6 $\mu\text{m}$ calculation		290579	290489	62.40	-90.36	-156.47	-152.76
Crystal parameters							
Crystal $T$	0.40 - 0.02 + 0.05 mm	0.00 (15)	4.50 (15)	0.00 (15)	4.50 (15)	4.80 (20)	4.50 (20)
Block width $t_0$	0.60 (3) $\mu\text{m}$	0.17 (15)	0.17 (15)	0.17 (15)	0.17 (15)	0.53 (20)	0.00 (20)
Mosaic angle width	0-10 <sup>-4</sup> rad	0.25 (15)	0.27 (15)	0.25 (15)	0.27 (15)	0.02 (20)	0.02 (20)
$\alpha_{\text{plane}}$	0.0 $\pm$ 1.45 $\times$ 10 <sup>-3</sup> rad	437	440	437	440	1.27 (40)	3.93 (40)
Crystal 2Rz	300.0 (1) mm	129	130	129	130	0.08(40)	0.11(40)
Crystal 2d	8.7358 (6) $\text{\AA}$	Included in $\Delta\lambda$ and form-factor uncertainties					
Atomic (O) site	-0.01937 (14) z	0	0	0.01 (15)	0.01 (15)	0.01 (15)	0.01 (15)
$f_1, f_2$ errors	$\pm$ 2%	0	0	0.68 (15)	0.50 (15)	0.56 (20)	0.18 (20)
Vertical curvature $\alpha_3 = 0 \pm 1.6 \times 10^{-5}$ rad		0	0	0	0	0	0
Spectrometer parameters: $w_0 = 0$ (2) mm, $w = \pm 5$ mm $\rightarrow$							
$\rightarrow \alpha_1 =$	0.0 $\pm$ 0.0184 rad	81.7 (1)	78.5 (1)	0.01 (15)	0.05 (15)	0.07 (20)	0.06 (20)
$\beta = 0.1360$ , flamb* = 0 $\pm$ 1, $\alpha_{\text{Bm}} = 0.00$ (2), effect via							
$\Delta\lambda/\lambda$	0.0 $\pm$ 0.0025	1104	1104	0.54 (15)	0.90 (15)	0.28 (20)	0.36 (20)
Polarization, % $\sigma_{\text{out}}$	0.0 $\pm$ 10%	-	-	+0.49 (15)	-0.04 (15)	-	-0.53 (20)
Voigt fitting shift (to be subtracted)	(1 mm scan height) (0.45 mm height)	-0.37 (49)	+2.58 (43)	-0.37 (49)	+2.58 (43)	+2.32 (43)	+2.95 (65)
2Rzf	300.0 (1) mm	129.0 (1)	129.0 (1)	129.0 (1)	129.0 (1)	0.04 (20)	0.12 (20)
Cx	0.00 (3) mm	166	166.1 (2)	166	166.1 (2)	0.03 (20)	0.00 (20)

(b) Effect of crystal thickness  $T = 0.1524$  mm (versus 0.4 mm): summary for the earlier experiment ( $\mu\text{m}$ ) (Silver *et al.*, 1987; McClelland, 1989)

Order, polarization	Value (Uncertainty)	1st, $\pi$ $Y_{iz}-Y_{oz}$ shift (Differential)	4th, $\pi$	4th-1st, $\sigma$ $Y_{iz}-Y_{iz}$ shift (Relative)	4th-1st, $\pi$
With respect to values		56.65	-37.73	-100.88	-94.38
0.6 $\mu\text{m}$ high-precision calculation		62.40	-37.73	-104.04	-100.13
Parameters					
Crystal $T$	0.1524 - 0.02 + 0.05 mm	0.00 (15)	12.49 (15)	12.53 (20)	12.49 (20)
Block width $t_0$	0.50-0.75? $\mu\text{m}$	0.14 (15)	0.31 (15)	0.99 (40)	0.45 (40)
Angular width	0-10 <sup>-3</sup> rad	2.5 (15)	2.7 (15)	0.2 (20)	0.2 (20)
$\beta = 0.1360$ (3), flamb* = 0 $\pm$ 1, $\alpha_{\text{Bm}} = 0.004$ (4)? rad, via					
$\Delta\lambda/\lambda$	0.000 (1)	0.22 (5)	0.36 (5)	0.11 (5)	0.14 (5)
Polarization, % $\sigma_{\text{out}}$	0 $\pm$ 10%	+0.49 (15)	-0.04 (15)	-	-0.53 (20)
Voigt fitting shift (to be subtracted)	1 mm height† 0.45 mm height†	+0.12 (47) +0.05 (44)	+0.03 (38) +0.32 (35)	+0.66 (60) +0.27 (56)	-0.09 (60) +0.27 (56)
2Rzf	300.00 (5) mm	64.5 (1)	64.5 (1)	0.02 (20)	0.06 (20)
Cx	0.0 (3) mm	1661 (1)	1661 (1)	0.30 (20)	0.00 (20)

(c) Additional width uncertainties and errors ( $\mu\text{m}$ ).

Order, polarization	Value with respect to 0.7 $\mu\text{m}$	1st, $\sigma$	1st, $\pi$	4th, $\sigma$	4th, $\pi$
0.4 mm values		244.1	288.7	179.8	175.0
Crystal $T$	0.40 - 0.02 + 0.05 mm	1 (2)	3 (2)	1 (2)	3 (2)
$\alpha_{\text{plane}}$	0 $\pm$ 1.45 $\times$ 10 <sup>-3</sup> rad	1 (2)	6 (2)	3 (2)	9 (2)
Crystal 2Rz	300.0 (1) mm	2 (2)	7 (2)	0 (2)	2 (2)
Detector 2Rzf	300.0 (1) mm	1 (2)	2 (2)	0 (2)	3 (2)
Cx	0.00 (3) mm	5.5 (2)	5 (2)	0 (2)	3 (2)

\* flamb is a variable representing the presence or absence of QED corrections to the wavelengths and hence adjusts the wavelengths by the value of the Lamb shift. This is a valid point because the Lamb shifts for the transitions involved have been measured only indirectly and with moderate precision. Nonetheless, it can be seen that this error is subsumed within the uncertainties of  $\beta$  and  $\alpha_{\text{Bm}}$ .

† Early analysis used single Gaussian fits of blended lines.

High-precision 0.6  $\mu\text{m}$  calculations are accurate to 0.2–0.4  $\mu\text{m}$ . Low-precision calculations (including some 0.7  $\mu\text{m}$  results, as indicated) introduce a 3–5  $\mu\text{m}$  first-order shift due to neglect of asymmetric weak contributions. Large fitting shifts are known robust systematic shifts and may be corrected for. The calculation precision is then better than that of centroids from the fitting routine ( $\pm 0.45 \mu\text{m}$ ). The latter may be improved by densitometry in 10  $\mu\text{m}$  steps compared with the present value of 20  $\mu\text{m}$ .

Tolerances on crystal thickness and diffracting-plane angle are critical but are the best values available from the suppliers. They give limiting uncertainties of 4.50 and 3.93  $\mu\text{m}$  in arc for the improved experiment, leading to 6  $\mu\text{m}$  in total or 13.8 parts in  $10^6$  in Lyman  $\alpha$  wavelengths and 2.4% of extracted Lamb shifts. Increased precision in this area could lead to submicrometre final accuracy. The earlier experiment with PET (Silver *et al.*, 1987; McClelland, 1989) is impaired by the large fractional uncertainty on the narrower crystal thickness [Table 4(b)], so shifts have an accuracy of only 13  $\mu\text{m}$ , 30.2 parts in  $10^6$  or 5.3% of extracted Lamb shifts. The earlier formed crystal-bending technique can introduce further errors and earlier analysis assumed infinite (flat) perfect crystal values with unpolarized diffracted radiation, as opposed to currently accepted values.

The result of this analysis is that the mosaic block width  $t_0 = 0.60$  (3)  $\mu\text{m}$  and the (Gaussian) angular misorientation half-width  $= 5$  (5)  $\times 10^{-5}$  rad are determined and the incident first-order (Balmer  $\beta$ ) radiation is (partially)  $\pi$ -polarized; the dominant broadening not included in the modelling is largely Lorentzian in character and corresponds to a beam divergence of  $\delta\theta = 8.4$  (63)  $\times 10^{-4}$  rad. The validity of the model is supported by the limited range of asymmetry allowed between first- and fourth-order profiles and the consistency of experimental data with these limits. Tests have also been performed on other crystals under similar conditions.

### 11. Application to ADP 101: reflectivities and profiles

Ammonium dihydrogen phosphate ( $\text{NH}_4\text{H}_2\text{PO}_4$ ) (ADP) crystallizes in the tetragonal space group  $I4_2d$ . X-ray and neutron crystallography has provided atomic locations, temperature factors and lattice parameters. Values reported by Tenzer, Frazer & Pepinski (1958) for neutron diffraction lead to  $2d_{101} = 10.640 \text{ \AA}$ , in contradiction with Burek (1976) (10.648  $\text{\AA}$ ). Khan & Baur (1973) give  $a = 7.4997$  (4),  $c = 7.5494$  (12)  $\text{\AA}$  at room temperature for X-ray diffraction, which is used here, giving  $2d_{101} = 10.64115$  (89)  $\text{\AA}$ , in agreement with other determinations. Use of X-ray coordinates for O atoms and

neutron values for H atoms gives agreement with Burek *et al.* (1974) for first and second orders.

Burek (1976) quotes theoretical integrated reflectivities for infinite flat perfect crystals of approximately  $8 \times 10^{-5}$ ,  $1.2 \times 10^{-5}$  and  $1.8 \times 10^{-5}$  for orders 1 to 3 in the iron Lyman–Balmer region. The current model estimates reflectivities of  $8.1 \times 10^{-5}$ ,  $1.37 \times 10^{-5}$ ,  $7.12 \times 10^{-6}$  and  $6.33 \times 10^{-6}$  for first to fourth orders in the finite flat crystal case, becoming  $9.35 \times 10^{-5}$ ,  $2.03 \times 10^{-5}$ ,  $2.99 \times 10^{-5}$  and  $6.05 \times 10^{-5}$  after curvature. Burek's values for PET reflectivities agree with the present infinite flat perfect crystal calculations. Curvature and mosaicity yield  $R_C(1)/R_C(4) = 20.63$ ,  $\pm 20\%$ , for PET from previous sections, which may be used to estimate agreement with theory for ADP. Experiments were performed with 0.4 mm thick ADP 101 crystals under identical conditions to the 0.4 mm thick PET crystal experiments discussed earlier and in paper I.

Experimentally,  $[R_C(1)/R_C(4)]_{\text{ADP}}/[R_C(1)/R_C(4)]_{\text{PET}} = 0.038$  (13), implying  $[R_C(1)/R_C(4)]_{\text{ADP}} = 0.784$  and a value for first-order radiation of  $4.7 \times 10^{-5}$  instead of the value of  $9.4 \times 10^{-5}$  above. The error is due to uncertainties in the experimental fitting of areas and their ratios, linearization uncertainty and uncertainty in theoretical ratios and mosaic character. Neglect of curvature would yield a first-order reflectivity of  $4.96 \times 10^{-6}$  in strong conflict with theory.

ADP has low reflectivity but is composed of only slightly higher  $Z$  atoms than PET. It is stiffer than PET, so should give decreased mosaic character, but over long time periods relaxation occurs. Crystals used in the experiment had sizes and tolerances as for PET in Table 4(a). The crystals do not cleave along the major diffracting planes, so their preparation requires solution polishing (Burek *et al.*, 1974). Deslattes, Torgeson, Paretzkin & Horton (1966) report double-crystal rocking-curve widths in consonance with perfect-crystal calculations, so that near perfection is certainly possible for unstressed crystals. The perfection was observed to deteriorate with exposure to water vapour, so storage in a desiccator prior to mounting and use is necessary. Stabilities of prepared crystals in width and reflectivity under normal conditions in (humid) air and during strong X-ray irradiation has been demonstrated (Burek, 1976), so this problem appears minor. Figs. 7 and 8 give ADP 101 diffraction profiles on the film and output angular scales, showing finite precision, *Pendellösung* oscillations, asymmetry and other details for standard lines across the film.

Fig. 9 illustrates different dominant contributions to systematic shifts and reflectivities for PET and ADP diffraction. PET shows clearly the dominance of the  $\tan \theta_B$  dependence from refractive-index shifts in first order, while ADP 101 first-order shifts and reflectivities are affected by the (polar)  $PK$  edge at

2.0–2.1 keV or 0.57 rad. Dominant contributions to PET third-, fourth- and fifth-order shifts approach the  $\cot \theta_B$  dependence of the low-absorption limit, with additional curvature from second-order  $\cot^2 \theta_B$  terms, with magnitude limited by the crystal thickness. Mosaicity introduces a small but significant shift by increasing depth penetration and shifting the centroid from  $-1 < y < 0$  to  $y \approx 0$ . Conversely, fourth-order ADP diffraction is dominated by absorption and

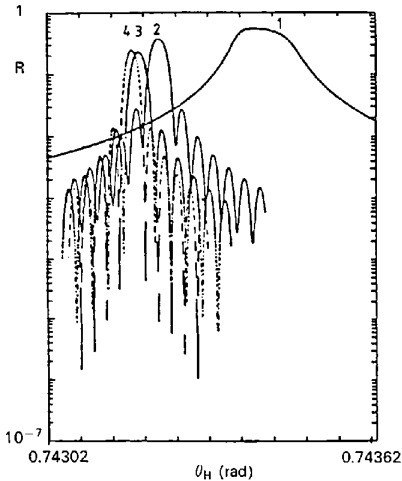


Fig. 7. Diffraction profiles for ADP (101) $n$  finite flat perfect crystals on the Bragg-angle scale for  $2Rz = 300$  mm,  $T = 0.4$  mm (wavelengths Doppler shifted by  $\beta = 0.136$ ). Profiles for  $7.2 \text{ \AA}/n$ ,  $n = 1-4$ ,  $\pi$ -polarized radiation.  $t_0 = 36.8-5.04 \text{ \mu m}$ .

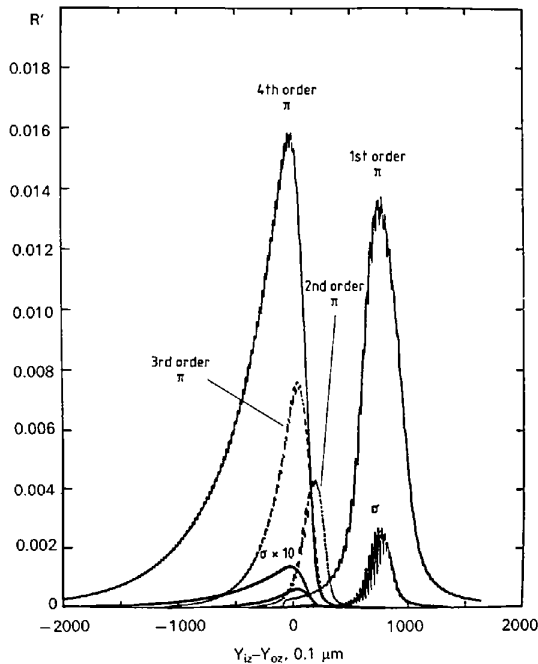


Fig. 8. Expected profiles for ADP (101) $n$  finite curved perfect crystal diffraction at  $7.2 \text{ \AA}/n$ ,  $n = 1-4$ , on the film ( $Y_{iz}$  scale,  $0.1 \text{ \mu m}$ ).  $T = 0.4$  mm,  $2Rz = 300$  mm.

the corresponding  $(1/\mu) \cos \theta_B \propto \cos \theta_B / \sin^3 \theta_B$  term [(12)], with significant contribution from second-order terms. Integrated reflectivities  $R_H^{0\beta}$  do not agree with the form of Burek (1976) (owing to effects of curvature) and show relative insensitivity to angle, except for the  $\cos 2\theta_B$  damping of  $\sigma$ -polarized radiation.

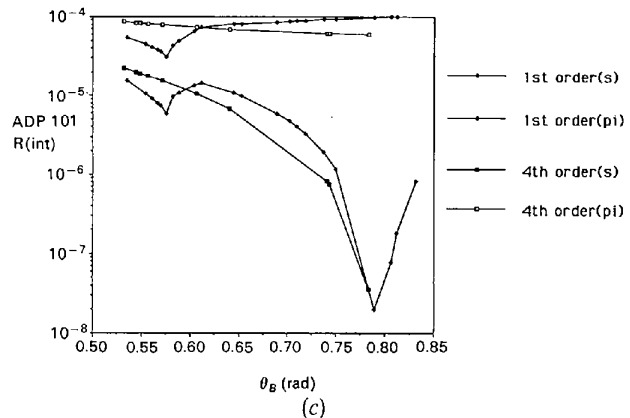
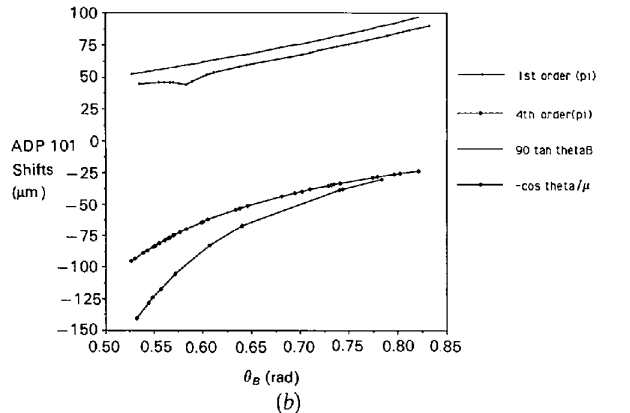
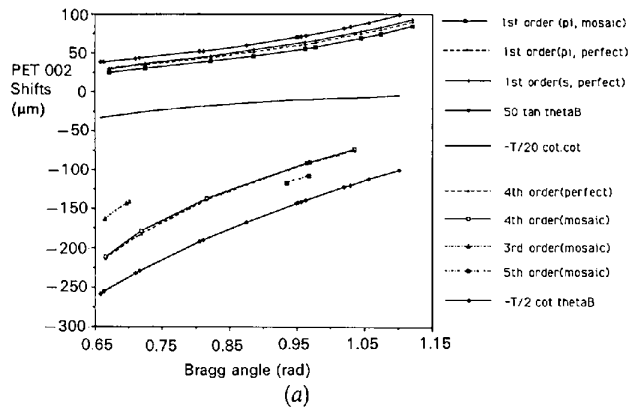


Fig. 9. Centroid shifts  $Y_{iz} - Y_{oz}$  ( $\mu\text{m}$ ) versus Bragg angle (rad) for (a) PET (002) $n$  and (b) ADP (101) $n$  crystal diffraction with  $2Rz = 300$  mm,  $T = 0.4$  mm. Perfect-crystal and (in a) mosaic-structure results are compared with leading contributions to shifts. (c) Integrated reflectivities  $R_H^{0\beta}$  versus Bragg angle (rad) for ADP (101) $n$  crystal diffraction with  $2Rz = 300$  mm,  $T = 0.4$  mm. Incident polarizations are compared.

Table 5. Summary of uncertainties and errors ( $\mu\text{m}$ )

Lyman  $\alpha$ -Balmer  $\beta$  region for ADP  $n0n$  diffraction,  $2Rz = 300$  mm at  $\lambda = 7.2$  Å/ $n$ ,  $n = 1-4$ , crystal  $2d = 10.6411$  (9) Å. Scaling:  $(\Delta\lambda/\lambda)/\Delta Y_{iz} = (3.68 \times 10^{-6}; 3.58 \times 10^{-6}) \mu\text{m}^{-1}$  (Ba  $\beta_{1-4}$ ; Ba  $\beta_{5-7}$ ).

Order, polarization	Value (Uncertainty)	1st, $\sigma$ $Y_{iz}-Y_{oz}$ shift (Differential)	1st, $\pi$ $Y_{iz}-Y_{oz}$ shift (Differential)	4th, $\sigma$ $Y_{iz}-Y_{oz}$ shift (Differential)	4th, $\pi$ $Y_{iz}-Y_{oz}$ shift (Differential)	4th-1st, $\sigma$ $Y_{iz}-Y_{iz}$ shift (Relative)	4th-1st, $\pi$ $Y_{iz}-Y_{iz}$ shift (Relative)
With respect to shifts		76.27	76.14	-35.93	-36.06	-112.20	-112.20
Low-precision f.c.p. crystal shifts		73.29 (15)	72.89 (15)	-36.07 (15)	-36.41 (15)	-109.36 (20)	-109.30 (20)
Emulsion shifts		0.859	0.859	5.60	5.60	-	-
Perfect-crystalline thicknesses ( $\mu\text{m}$ )		19.1	36.8	5.94	5.04	-	-
$R_C$ , f.f.p. crystals, $10^{-6}$ rad		0.96	82.3	0.057	6.37	-	-
$R_B^0$ , $10^{-6}$ rad		1.08	93.6	0.523	61.1	-	-
$Y_{iz}$ widths ( $\mu\text{m}$ )		21.0	35.3	50.4	50.2	-	-
Observed $w_T, w_G/w_T$ , crystal 1		232.1 $\pm$ 13.5, 0.65 $\pm$ 0.06		216.4 $\pm$ 5.5, 0.976 $\pm$ 0.01			
Observed $w_T, w_G/w_T$ , crystal 2		226.6 $\pm$ 7.8, 0.91 $\pm$ 0.03		220.6 $\pm$ 6.6, 0.93 $\pm$ 0.01			
Crystal parameters							
Crystal $T$	0.40-0.02 + 0.05 mm	0.00 (15)	0.00 (15)	0.03 (15)	0.02 (15)	0.03 (20)	0.02 (20)
Block width $t_0$	' $\infty$ '					0?	0?
$\alpha_{\text{plane}}$	$0 \pm 1.45 \times 10^{-3}$ rad	435.5	436.3	437.9	437.6	+2.40 (20)	+1.30 (20)
Crystal $2Rz$	300.0 (1) mm	-127.83	-127.84	-127.87	-127.94	-0.04 (20)	-0.10 (20)
Atomic (O) site	0.0843 (7)	0.00 (15)	0.43 (15)	0.06 (15)	0.03 (15)	-0.06 (20)	+0.46 (20)
$f_1, f_2$ errors	$\pm 2\%$	-0.35 (15)	-0.35 (15)	-0.70 (15)	-0.71 (15)	-0.35 (20)	-0.36 (20)
Spectrometer parameters: $w_0 = 0$ (2) mm, $w = \pm 5$ mm $\rightarrow$							
$\rightarrow \alpha_1 =$	$0.0 \pm 0.0184$ rad	0.03 (15)	0.02 (15)	0.00 (15)	0.01 (15)	0.03 (20)	0.03 (20)
$\beta = 0.1360$ (3), flamb = $0 \pm 1$ , $\alpha_{Bm} = 0.00$ (2) rad, effect via							
$\Delta\lambda/\lambda$	$0.0 \pm 0.0025$	0.27 (15)	0.04 (15)	0.57 (15)	0.52 (15)	0.30 (20)	0.48 (20)
Polarization, % $\sigma_{\text{out}}$	0.0 (8)%		1.0E - 3		1.0E - 3		0.0E - 3
Voigt fitting shift (to be subtracted)	(1 mm scan height) (0.40 mm height)	0.00 (34) -0.07 (30)	0.00 (35) -0.02 (32)	+2.64 (37) +4.06 (35)	+2.71 (37) +3.94 (35)	+2.64 (50) +4.13 (46)	+2.71 (51) +3.96 (47)
3rd-order Ly $\alpha$	(0.40 mm height)			+6.77 (27)	+6.79 (27)		
2Rzf	300.0 (1) mm	127.77	127.79	127.79	127.81	+0.02 (20)	+0.02 (20)
Cx	0.00 (3) mm	145.83	145.86	145.93	145.96	+0.10 (20)	+0.10 (20)

## 12. Effects on shifts of crystal and spectrometer parameters: ADP 101

The Lyman  $\alpha$ -Balmer  $\beta$  region in ADP has a Bragg angle near to  $45^\circ$ , so  $\sigma$  radiation is dampened enormously. The PET result for polarization, under identical conditions, implies that diffracted radiation is purely  $\pi$  polarized ( $< 0.8\%$   $\sigma$  contribution). The crystal-thickness uncertainty is not dominant owing to decreased depth penetration for all orders (from the higher- $Z$  elements composing the crystal). The resolution for first-order finite curved perfect crystal diffraction is increased by a factor of two. Observed widths are dominated by other factors (possibly including mosaicity).

Dominant uncertainties in theoretical shifts are due to  $\alpha_{\text{plane}}$ , fitting shifts,  $\alpha_{Bm}$  and the computational precision, totalling 5.6 parts in  $10^6$  of Lyman  $\alpha$  wavelengths or a Lamb-shift uncertainty of 0.98%. Signs of width uncertainties show that the Rowland circle is not the location with best resolution for a Johann geometry.

The perfect-crystal calculation implies that equal densities of Lyman lines (for ADP versus PET diffraction) require halved exposures, while first-order lines need 6.7 times longer exposure. Both values may be

adjusted for mosaicity but this ratio was observed experimentally. Longer exposures approach saturation of Lyman lines and hence may lead to null measurements (in addition to requiring more time on the accelerator). The signal-to-noise ratio is extremely good for Lyman components but is poor for Balmer components and limits the final precision. A future experiment should optimize the exposure time. Resulting QED measurements indicate agreement of diffraction shifts to within quoted uncertainties, and hence support conclusions regarding PET diffracted polarization and the mosaic and perfect curved crystal models. Other support arises from observed relative intensities of diffracted lines.

Mosaicity of crystals used is not well defined by the data, owing to the influence of strong calibration and Lyman  $\alpha$  profile tails on weak Balmer peaks with relatively large noise. Fitted Lyman widths in the best data must be increased by 15-25% owing to a photographic effect of order overlap on linearization (Chantler, 1990). Widths are given in Table 5 for the two crystals used. Balmer widths of both crystals are in reasonable agreement with one another and with Lyman widths, and also with less precise data. Within significant uncertainty, results are consistent with symmetric broadening of perfect curved crystals by

defocusing, divergence and other effects. They are also consistent with slight mosaic character. Mosaic parameters would need to be determined from further experiments where broadening should be minimized. This test demonstrates that perfect curved crystal behaviour can be observed (to this precision) in real crystals and that this limit of the model is valid.

### 13. Application to silicon 111 and the germanium experiment

Silicon is the most fully tested crystal owing to industrial applications and the perfection of the lattice structure. Standard texts give the space group  $Fd\bar{3}m$ . Lattice spacings are known more precisely for silicon than any other crystal [ $2d_{111} = 6.2712108(30) \text{ \AA}$  (Caciuffo, Melone, Rustichelli & Boeuf, 1987)] and are in good agreement with different samples (Aldred & Hart, 1973) [ $2d_{111} = 6.271251245 \text{ \AA} + 2.53 \times 10^{-6} \text{ \AA K}^{-1}$  at 291 K (Deslattes, 1980)]. The crystal structure is simple, reducing form and structure-factor uncertainties compared with hydrogenous crystals. Double-crystal profiles with Si 111 and quartz crystals define the shape and width and the influence of dislocations (Bearden, Marzolf & Thomsen, 1968). These are in rough agreement with single-crystal values given here for first-order radiation (Figs. 10 and 11).

Experiments have been performed to compare hydrogenic germanium spectral lines in first-order (Balmer  $\beta$ ,  $\lambda \approx 4.644\text{--}4.742 \text{ \AA}$ ) and fourth-order (Lyman  $\alpha$ ,  $\lambda \approx 1.167\text{--}1.172 \text{ \AA}$ ) diffraction from Si (111) $n$  crystal planes in a Rowland-circle geometry

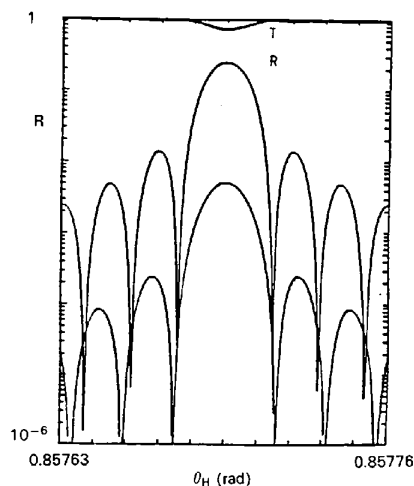


Fig. 10. Flat perfect crystal profiles for Si 111 on the Bragg-angle scale, for  $2Rz = 300 \text{ mm}$ , crystal thickness  $0.4 \text{ mm}$ ,  $\beta = 0.1774$ . Reflection and transmission coefficients for  $\sigma$  and  $\pi$  radiations of selected lines of hydrogenic germanium. Profiles for Lyman  $\alpha_1$  radiation ( $\lambda_D = 1.186 \text{ \AA}$ ) in fourth order.

with a finite source,  $2Rz = 300 \text{ mm}$ ,  $T = 0.1524 \text{ mm}$  and photographic detection (Chantler, 1990). Secondary peaks included third-, fourth- and fifth-order diffraction of the Lyman series, first-order diffraction of the Balmer series and helium-like satellite peaks. These peaks yield independent Doppler-free calibration of spectrometer and detector geometries subject to correct allowance for diffraction shifts of centroids. The germanium experiment used the formed mounting technique and the focus was not measured interferometrically (it was an earlier experiment than PET and ADP measurements), so alignment and other variables are less well defined (Laming *et al.*, 1988; Laming, 1988). Earlier diffraction corrections are mentioned in paper I.

Germanium Lyman  $\alpha$  radiation in fourth order diffracts at  $0.86 \text{ rad} = 49.3^\circ$  for Si 111, so  $\sigma$ -polarized radiation is strongly damped. Polarization ratios are unclear and  $\pi$ -polarized radiation is assumed, with the same precision as for iron X-rays diffracted from PET crystals. Defocusing and mosaic broadening is assumed to be  $100 \mu\text{m}$  of Lorentzian character. This is an underestimate, leading to overestimated fitting shifts. However, the small crystal thickness and near-symmetric profiles lead to small error contributions from this source.

The  $0.1524 \text{ mm}$  thickness used gives the dominant uncertainty in the calculations, followed by that of

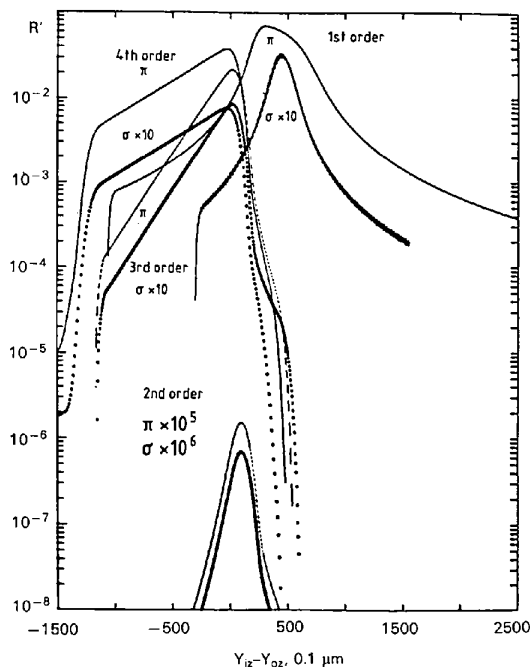


Fig. 11. Curved perfect crystal profiles for Si  $nmn$  at  $4.7554 \text{ \AA}/n$ ,  $n = 1\text{--}4$ , on the film ( $Y_{iz}$  scale,  $0.1 \mu\text{m}$ ).  $T = 0.1524 \text{ mm}$ ,  $2Rz = 300 \text{ mm}$ . Note the near extinction of second-order diffraction.

$\alpha_{\text{plane}}$  and the precision of calculation. The atomic site contributes no uncertainty. The resulting accuracy is approximately  $3.2 \mu\text{m}$  on the detector location,  $9.2$  parts in  $10^6$  of the wavelengths or  $1.2\%$  of extracted hydrogenic Lamb shifts.

Reflectivities may be compared to experiment and to intensities from lithium-drifted silicon detector measurements, subject to linearization of photographic densities. Profiles and widths are in rough agreement but additional convolution is required to yield experimental profiles. Shifts agree at approximately the  $10\%$  level, but further direct measurement (with minimal additional broadening) would be valuable. First-order shifts are again dominated by refractive-index corrections while fourth-order shifts require inclusion of several secondary effects (Fig. 12). Reflectivities display the  $\cos 2\theta_B$  dependence for  $\sigma$  polarization. Results are in qualitative agreement with perfect double-crystal estimates within quoted uncertainty, allowing for curvature and other effects (Burek, 1976), with asymmetric infinite crystal diffraction calculations (Caciuffo *et al.*, 1987) and with other calculations and measurements (Suortti,

Pattison & Weyrich, 1986; Chukhovskii, Gabrielyan, Kislovskii & Prokopenko, 1987; Erola, Eteläniemi, Suortti, Pattison & Thomlinson, 1990), after allowance is made for developments reported here and in paper I.

Profiles display the need to define lamellar thicknesses in a consistent manner with respect to finite thickness widths and  $\Delta y$  values, allowing for coherence between (truncated) lamellae, especially for higher-order diffraction. The importance of correct allowance for depth penetration and other diffraction effects is also clear, requiring a method that does not involve periodic error of the order of the lamellar thickness and is accurate to a fraction of this thickness. Incoherent scattering is less important for silicon than for other crystals investigated in this energy range (see paper I).

Mosaic parameters for this crystal are not investigated in detail owing to the dominance of curvature on reflectivities and centroid shifts. Experimental first-order profiles are broader than corresponding fourth-order profiles, consistent with the introduction of mosaic character on bending and mosaic block sizes of order  $1 \mu\text{m}$  (Laming, 1988, p. 62). The two crystals used had very different Balmer widths with similar Lyman widths, implying different states of mosaicity. Defocusing, satellite and fitting errors are unable to account for this broadening. Crystal 1 appears consistent with a mosaic block size of about  $0.8 \mu\text{m}$ , while crystal 2 appears to correspond to  $t_0 \approx 0.4 \mu\text{m}$  (Table 6). This is due to the formed mounting method of bending the crystals, not used in subsequent experiments. The effect of this mosaicity on  $Y_{iz}$  centroid shifts is less than  $2 \mu\text{m}$ , which is a small but significant additional contribution to final results. Reflectivities are affected at the  $25\%$  level for first-order radiation (and less for fourth-order radiation) so only profiles and widths are strongly affected by this character.

The data may be used to test bending methods rather than the model and theory. Here, the formed method impresses the curvature on the crystal and imprecision of the base and front plate with uneven tightening of screws leads to non-uniform stress, curvature and induced mosaicity. The scale of mosaicity induced is uncertain, as observed in the data. Alternative (two-point, two-bar) bending methods used for PET and ADP experiments may also induce mosaicity for soft or plastic crystals as a necessary consequence of the stress. However, this is apparently minimized and is uniform for different crystals and exposures separated by several days. Initial relaxation occurs, but subsequent dislocation over the time scale of current experiments is minimal. Results from wavelengths diffracting in similar regions in different orders from crystal planes enable significant mosaicity, if present, to be quantified.

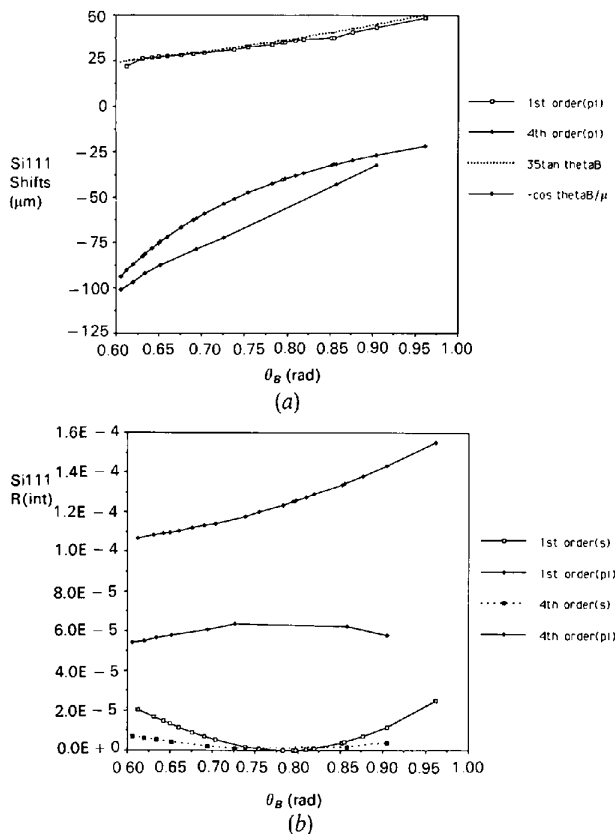


Fig. 12. (a) Centroid shifts  $Y_{iz} - Y_{oz}$  ( $\mu\text{m}$ ) and (b) integrated reflectivities  $R_H^2$  versus Bragg angle (rad) for Si (111) $n$  crystal diffraction with  $2Rz = 300 \text{ mm}$ ,  $T = 0.4 \text{ mm}$ . In (a) perfect-crystal results are compared with leading contributions to shifts; in (b) incident polarizations are compared.

Table 6. *Uncertainties for the germanium experiment* ( $\mu\text{m}$ )

Laming *et al.* (1988); Laming (1988);  $\lambda = 4.755427 \text{ \AA}/n$ ,  $n = 1, 4$ ,  $2d = 6.271251 (6) \text{ \AA}$ . Lyman  $\alpha$ -Balmer  $\beta$  region for Si  $nmn$  diffraction,  $2Rz = 300 \text{ mm}$ . Scaling:  $(\Delta\lambda/\lambda)/\Delta Y_{iz} = (2.915 \times 10^{-6} - 2.793 \times 10^{-6}) \mu\text{m}^{-1}$ .

Order, polarization	Value (Uncertainty)	1st, $\sigma$ $Y_{iz}-Y_{oz}$ shift (Differential)	1st, $\pi$	4th, $\sigma$	4th, $\pi$ $Y_{iz}-Y_{oz}$ shift (Differential)	4th-1st, $\sigma$ $Y_{iz}-Y_{iz}$ shift (Relative)	4th-1st, $\pi$
With respect to f.c.p. crystal shifts, $T = 0.1524 \text{ mm}$		44.31	42.27	-31.54	-31.64	-75.85	-73.91
Intermediate precision, $T = 0.1524 \text{ mm}$		43.46	41.36	-31.50	-31.60	-74.96	-72.96
Tests, low precision, $T = 0.1524 \text{ mm}$		40.37	38.09	-31.54	-31.64	-71.91	-69.73
Low precision, $T = 0.40 \text{ mm}$		40.37	38.09	-42.11	-42.12	-82.48	-80.21
Emulsion shifts		1.92	1.92	5.03	5.03	-	-
Perfect-crystalline thicknesses, $\mu\text{m}$		31.9	63.3	4.43	5.03	-	-
$R_C$ , f.f.p. crystals ( $10^{-6} \text{ rad}$ )		4.13	123	0.104	4.81	-	-
$R_H^2$ ( $10^{-6} \text{ rad}$ )		4.62	135	1.47	57.3	-	-
$Y_{iz}$ f.c.p. crystal widths ( $\mu\text{m}$ )		20.5	46.9	47.2	48.1	-	-
$w_T, w_G/w_T$ calculation with $100 \mu\text{m } L, 75.5 \mu\text{m } S$		137.9 (7),	0.835 (6)	144.6 (7),	0.889 (6)		
Observed $w_T, w_G/w_T$ , crystal 1 ( $t_0 \approx 0.8 \mu\text{m}$ )		260.1 (50),	0.66 (4)	215.6 (47),	0.76 (2)		
Observed $w_T, w_G/w_T$ , crystal 2 ( $t_0 \approx 0.4 \mu\text{m}$ )		349.2 (39),	0.60 (3)	235.1 (28),	0.914 (7)		
Effect on widths							
Crystal $T$	0.1524 - 0.02 + 0.05 mm	0.0 (5)	-0.1 (5)	+0.4 (5)	0.0 (5)		
$\alpha_{\text{plane}}$	$0.0 \pm 1.45 \times 10^{-3} \text{ rad}$	0.5 (5)	-2.0 (5)	-0.4 (5)	-0.3 (5)		
$2Rzf$	300.0 (1) mm	+0.3 (5)	-0.1 (5)	+0.1 (5)	+0.1 (5)		
Crystal parameters, effect on shifts							
Crystal $T$	0.1524 - 0.02 + 0.05 mm	0.00 (20)	0.00 (20)	2.71 (20)	2.74 (20)	2.71 (30)	2.74 (30)
$\alpha_{\text{plane}}$	$0 \pm 1.45 \times 10^{-3} \text{ rad}$	437.04	436.24	437.44	437.44	+0.75 (30)	+1.50 (30)
Crystal $2Rz$	300.1 (1) mm	128.21	127.14	127.46	127.16	+0.75 (30)	-0.02 (30)
$f_1, f_2$ errors	$\pm 2\%$	+0.02	+0.07	-0.04	-0.13	-0.06 (30)	-0.20 (30)
Spectrometer parameters, effect on shifts: $w_0 = 0 (2) \text{ mm}, w = \pm 5 \text{ mm} \rightarrow$							
$\rightarrow \alpha_1$	$0 \pm 0.0184 \text{ rad}$	-0.29	-0.28	-0.89	-0.55	-0.60 (30)	-0.27 (30)
$\beta = 0.1772 (3)$ , flamb = $0 \pm 1, \alpha_{\text{Bm}} = 0.00 (2)? \text{ rad}$ , effect via							
$\Delta\lambda/\lambda$	$0.0 \pm 0.0025?$	+0.57	+1.43	+1.11	+1.11	+0.54 (30)	-0.32 (30)
Polarization, % $\sigma_{\text{out}}$	$0 \pm 10\%$		0.20		0.01		+0.19
Voigt fitting shift (to be subtracted)	(1 mm scan height) (0.40 mm height)	-0.09 (26) +0.02 (23)	-0.03 (26) -0.39 (24)	-0.18 (29) +1.18 (24)	-0.14 (29) +1.12 (24)	-0.09 (39) +1.16 (34)	-0.11 (39) +1.51 (34)
3rd-order Ly $\alpha$	(0.40 mm height)			+9.39 (26)	+9.17 (26)		
$2Rzf$	300.0 (1) mm	+127.14	+127.04	+127.24	+127.23	+0.10 (30)	+0.19 (30)
Cx	0.0 (3) mm	+151.54	+151.54	+151.54	+151.54	+0.00 (30)	+0.00 (30)

#### 14. Summary

The new model corrects several earlier omissions in theory, applies to non-ideally imperfect crystals and more ideal or perfect regimes and has been verified in a range of computational, comparative and experimental tests. Semi-empirical relations generalized in (4)–(7) may be compared with the model in specific regimes. Model and crystal functions of reflectivity and diffraction shifts with angle and other variables have been explained in terms of simple relations for refractive-index and depth-penetration corrections, with more complex secondary contributions for particular orders of diffraction. Dependence of these parameters and widths on mosaicity and curvature have been illustrated.

The form of this dependence agrees with experiment for near-perfect (ADP), intermediate (PET) and nearly ideally imperfect crystals (Si) and has been used to derive mosaic and experimental parameters within

narrow limits. Consequently, diffraction and other systematic shifts may be accurately predicted. Uncertainties from experimental parameters have been computed and tabulated for three systems investigated in iron and germanium Lyman  $\alpha$  and Balmer  $\beta$  QED measurements.

Results confirm that formed mounting methods should be rejected in favour of more advanced and precise two-point two-bar or four-bar methods and that crystal thicknesses should generally be maximized to reduce consequent uncertainty in final shifts. The experiments, as presented, allow Lyman  $\alpha$  measurements, partially limited by diffraction uncertainties, at the 13.8, 30.2, 5.6 and 9.2 parts in  $10^6$  level. These can clearly be improved upon by minimizing tolerances on thicknesses, angular alignment of diffracting planes and experimental variables. However, with the exception of the second value quoted, these uncertainties lie at or below the best results reported thus far in the literature.

The author would like to thank Shell Australia, the Hasselblad Foundation and the Draper's Company for scholarships and fellowships relating to this research, and St Anne's College, Oxford, for a Junior Research Fellowship covering part of the period of research. Acknowledgements go to Drs J. D. Silver, D. D. Dietrich and J. M. Laming for assistance and support, especially on the experimental side of this work; to collaborations with Drs A. F. McClelland, P. H. Mokler, E. C. Finch, S. D. Rosner, R. MacDonald, and W. A. Hallett; and to A. J. Varney for helpful comments.

### References

- ALDRED, P. J. E. & HART, M. (1973). *Proc. R. Soc. London Ser. A*, **332**, 223–228.
- AL HADDAD, M. & BECKER, P. J. (1988). *Acta Cryst.* **A44**, 262–270.
- BACHMAN, K. J., BALDWIN, T. O. & YOUNG, F. W. JR (1970). *J. Appl. Phys.* **41**, 4783–4789.
- BATTERMAN, B. W. (1959). *J. Appl. Phys.* **30**, 508–513.
- BEARDEN, J. A., MARZOLF, J. G. & THOMSEN, J. S. (1968). *Acta Cryst.* **A24**, 295–301.
- BECKER, P. J. & AL HADDAD, M. (1990). *Acta Cryst.* **A46**, 123–129.
- BECKER, P. J. & COPPENS, P. (1974). *Acta Cryst.* **A30**, 129–147, 148–153.
- BROWN, D. B. & FATEMI, M. (1974). *J. Appl. Phys.* **45**, 1544–1554.
- BROWN, D. B., FATEMI, M. & BIRKS, L. S. (1974). *J. Appl. Phys.* **45**, 1555–1561.
- BUREK, A. (1976). *Space Sci. Instrum.* **2**, 53–104.
- BUREK, A. J., BARRUS, D. M. & BLAKE, R. L. (1974). *Astrophys. J.* **191**, 533–543.
- BUSHUEV, V. A. (1989). *Sov. Phys. Crystallogr.* **34**, 163–167.
- CACIUFFO, R., MELONE, S., RUSTICHELLI, F. & BOEUF, A. (1987). *Phys. Rep.* **152**, 1–71.
- CHANTLER, C. T. (1990). DPhil thesis, Univ. of Oxford, England.
- CHANTLER, C. T. (1992). *J. Appl. Cryst.* **25**, 674–693.
- CHANTLER, C. T., LAMING, J. M., SILVER, J. D., DIETRICH, D. D. & HALLETT, W. A. (1992). In preparation.
- CHUKHOVSKII, F. N., GABRIELIAN, K. T., KISLOVSKII, E. N. & PROKOPENKO, I. V. (1987). *Phys. Status Solidi A*, **103**, 381–387.
- COLE, H., STEMPLE, N. R. (1962). *J. Appl. Phys.* **33**, 2227–2233.
- DESLATTES, R. D. (1980). *Ann. Phys. (NY)*, **129**, 378–434.
- DESLATTES, R. D., TORGESON, J. L., PARETZKIN, B. & HORTON, A. T. (1966). *J. Appl. Phys.* **37**, 541–548.
- EROLA, E., ETELÄNIEMI, V., SUORTTI, P., PATTISON, P. & THOMLINSON, W. (1990). *J. Appl. Cryst.* **23**, 35–42.
- GUIGAY, J. P. (1989). *Acta Cryst.* **A45**, 241–244.
- HIRSCH, P. B. & RAMACHANDRAN, G. N. (1950). *Acta Cryst.* **3**, 187–194.
- KALMAN, Z. H. & WEISSMANN, S. (1983). *J. Appl. Cryst.* **16**, 295–303.
- KATO, N. (1980a). *Acta Cryst.* **A36**, 763–769.
- KATO, N. (1980b). *Acta Cryst.* **A36**, 770–778.
- KHAN, A. A. & BAUR, W. H. (1973). *Acta Cryst.* **B29**, 2721–2725.
- LAMING, J. M. (1988). DPhil thesis, Univ. of Oxford, England.
- LAMING, J. M., CHANTLER, C. T., SILVER, J. D., DIETRICH, D. D., FINCH, E. C., MOKLER, P. H. & ROSNER, S. D. (1988). *Nucl. Instrum. Methods Phys. Res.* **B31**, 21–23.
- MCCLELLAND, A. F. (1989). DPhil thesis, Univ. of Oxford, England.
- PATEL, J. R., WAGNER, R. S. & MOSS, S. (1962). *Acta Metall.* **10**, 759–764.
- PUNEGOV, V. I. (1990). *Sov. Phys. Crystallogr.* **35**, 336–340.
- SILVER, J. D., MCCLELLAND, A. F., LAMING, J. M., ROSNER, S. D., CHANDLER, G. C., DIETRICH, D. D. & EGAN, P. O. (1987). *Phys. Rev. A*, **36**, 1515–1518.
- SUORTTI, P., PATTISON, P. & WEYRICH, W. (1986). *J. Appl. Cryst.* **19**, 336–342.
- TENZER, L., FRAZER, B. C. & PEPINSKI, R. (1958). *Acta Cryst.* **11**, 505–509.
- ZACHARIASEN, W. H. (1945). *Theory of X-ray Diffraction in Crystals*. New York: Wiley.